Research Article

Nano Research
2024, 17(4): 3232–3244

ISSN 1998-0124 CN 11-5974/O4
https://doi.org/10.1007/s12274-023-6196-7

Modulating p-type doping of two-dimensional material palladium diselenide

Jiali Yang[1,3,§], Yu Liu[4,5,§], En-Yang Wang[10,§], Jinbo Pang[1,3] (✉), Shirong Huang[15,16,17,18], Thomas Gemming[2], Jinshun Bi[6,7,8] (✉), Alicja Bachmatiuk[9], Hao Jia[3], Shu-Xian Hu[10] (✉), Chongyun Jiang[11], Hong Liu[1,14] (✉), Gianaurelio Cuniberti[15,16,17,18] (✉), Weijia Zhou[1], and Mark H Rümmeli[2,4,5,12,13] (✉)

[1] *Institute for Advanced Interdisciplinary Research (iAIR), University of Jinan, Jinan 250022, China*
[2] *Institute for Materials Chemistry, Leibniz Institute for Solid State and Materials Research Dresden (IFW Dresden), 20 Helmholtz Strasse, Dresden 01069, Germany*
[3] *State Key Lab of Transducer Technology, Shanghai Institute of Microsystem and Information Technology, Chinese Academy of Sciences, Shanghai 200050, China*
[4] *College of Energy, Soochow Institute for Energy and Materials Innovations Soochow University, Suzhou 215006, China*
[5] *Key Laboratory of Advanced Carbon Materials and Wearable Energy Technologies of Jiangsu Province, Soochow University, Suzhou 215006, China*
[6] *School of Integrated Circuits, University of Chinese Academy of Sciences, Beijing 101408, China*
[7] *Institute of Microelectronics of Tianjin Binhai New Area, Tianjin 300451, China*
[8] *Institute of Microelectronics, Chinese Academy of Sciences, Beijing 100029, China*
[9] *Lukasiewicz Research Network, PORT Polish Center for Technology Development, Stablowicka 147, Wroclaw 54-066, Poland*
[10] *School of Mathematics and Physics, University of Science and Technology Beijing, Beijing 100083, China*
[11] *College of electronic information and optical engineering, Nankai University, Tianjin 300350, China*
[12] *Centre of Polymer and Carbon Materials, Polish Academy of Sciences, M. Curie Sklodowskiej 34, Zabrze 41-819, Poland*
[13] *Center for Energy and Environmental Technologies, VŠB-Technical University of Ostrava, 17. Listopadu 15, Ostrava 708 33, Czech Republic*
[14] *State Key Laboratory of Crystal Materials, Center of Bio & Micro/Nano Functional Materials, Shandong University, Jinan 250100, China*
[15] *Dresden Center for Computational Materials Science, Technische Universität Dresden, Dresden 01062, Germany*
[16] *Dresden Center for Intelligent Materials (GCL DCIM), Technische Universität Dresden, Dresden 01062, Germany*
[17] *Institute for Materials Science and Max Bergmann Center of Biomaterials, Technische Universität Dresden, Dresden 01069, Germany*
[18] *Center for Advancing Electronics Dresden, Technische Universität Dresden, Dresden 01069, Germany*
[§] *Jiali Yang, Yu Liu, and En-Yang Wang contributed equally to this work.*

Received: 7 August 2023 / **Revised:** 11 September 2023 / **Accepted:** 12 September 2023

ABSTRACT

The van der Waals heterostructures have evolved as novel materials for complementing the Si-based semiconductor technologies. Group-10 noble metal dichalcogenides (e.g., PtS_2, $PtSe_2$, PdS_2, and $PdSe_2$) have been listed into two-dimensional (2D) materials toolkit to assemble van der Waals heterostructures. Among them, $PdSe_2$ demonstrates advantages of high stability in air, high mobility, and wide tunable bandgap. However, the regulation of p-type doping of $PdSe_2$ remains unsolved problem prior to fabricating p–n junction as a fundamental platform of semiconductor physics. Besides, a quantitative method for the controllable doping of $PdSe_2$ is yet to be reported. In this study, the doping level of $PdSe_2$ was correlated with the concentration of Lewis acids, for example, $SnCl_4$, used for soaking. Considering the transfer characteristics, the threshold voltage (the gate voltage corresponding to the minimum drain current) increased after $SnCl_4$ soaking treatment. $PdSe_2$ transistors were soaked in $SnCl_4$ solutions with five different concentrations. The threshold voltages from the as-obtained transfer curves were extracted for linear fitting to the threshold voltage versus doping concentration correlation equation. This study provides in-depth insights into the controllable p-type doping of $PdSe_2$. It may also push forward the research of the regulation of conductivity behaviors of 2D materials.

KEYWORDS

two-dimensional (2D) materials, Lewis acid treatment, p-type doping, field-effect transistors, transfer characteristic

1 Introduction

Two-dimensional (2D) materials, such as graphene [1, 2] and MoS_2 [3], have facilitated the production of atomically thin transistors and van der Waals heterostructures. They are increasingly used in diverse applications, including defect engineering [4], exciton dynamics [5], and organic/inorganic heterointerfaces [6]. However, difficulties in bandgap opening and manipulation limit the transistor applications of graphene. The

Address correspondence to Jinbo Pang, ifc_pangjb@ujn.edu.cn; Jinshun Bi, bijinshun@ucas.ac.cn; Shu-Xian Hu, hushuxian@csrc.ac.cn; Hong Liu, hongliu@sdu.edu.cn; Gianaurelio Cuniberti, gianaurelio.cuniberti@tu-dresden.de; Mark H Rümmeli, m.ruemmeli@ifw-dresden.de

direct bandgap of monolayer MoS_2 limits its optoelectronic applications [7]. Junctions of two types of materials with arbitrary bandgaps are in high demand for application in optoelectronic devices. For example, a type-I heterojunction affords a combination of electron–hole pairs, enabling electroluminance [8–10]. In contrast, the use of type-II heterojunctions leads to the separation of charge carriers in photovoltaic devices and solar cells [11–13]. The van der Waals heterostructures show advantages of self-powered photodetectors [14]. Another anisotropic 2D material ReS_2 exhibits excellent electrochemical catalysis [15] and energy storage performances [16, 17], as well as stimuli-response upon water [18, 19] and heat [20]. It can be assembled with edge orientation [21] and doped for magnetism [22]. The ReS_2 has potential applications of sensing and therapy [23]. The anisotropic etching [24, 25] and epitaxial growth [26] become significant for heterostructure fabrication [27]. The power consumption should be investigated to utilize the advantage of 2D materials [28]. Again, the chemical vapor deposition continues to scale up the production of 2D materials [29–31].

Then, the library of materials that satisfy these requirements is confined to black phosphorus and noble metal dichalcogenides (NMDCs) [32], including PtS_2, $PtSe_2$, PdS_2, and $PdSe_2$. The bandgap of black phosphorus can be continuously tuned [33, 34] from 0.3 to 1.59 eV [35] by reducing its thickness from bulk [36] to monolayer phosphorene. However, as 2D materials are affected by oxygen and humidity, a passivation layer [37, 38] is necessary for their efficient operation, which introduces complexity in standard operation protocols. Chemical vapor deposition-grown PtS_2 does not exhibit a uniform phase and comprises mixed phases with PtS. PdS_2 may be subjected to sulfur loss, which alters its stoichiometric ratio [39].

Therefore, $PdSe_2$ has emerged as an ideal candidate for engineering and manufacturing optoelectrical devices with tunable bandgaps and air stability [40]. It has attracted significant attention for applications involving direct growth over dielectrics via chemical vapor deposition [41–44], metal selenization [45], nanoribbon formation [46], doping and phase transformation via plasma treatment [47–49], and layer-by-layer thinning [50, 51]. New trends emerge, such as vapor phase growth [52] or epitaxy over template [53]. Owing to its air stability [54], high mobility [55, 56], and broad tunable bandgap (0–1.3 eV) [57], $PdSe_2$ has promising application prospects in conventional semiconductor physics, as a channel material or saturable absorber for utilization in electronics [58, 59], thermoelectrics [60], ultrafast photonics [61–64], and optoelectronics [65–68]. The conductance characteristics of a $PdSe_2$-based field-effect transistor (FET) can be regulated from n-type to p-type by changing the pressure of the sealed FET chamber from vacuum conditions (0.01 atm) to 0.2 atm and again to 1 atm under an N_2 atmosphere [69]. In addition, electron irradiation (10 keV) can change the transfer characteristics from n- to p-type [70]. Under vacuum conditions, $PdSe_2$ remains as an n-type material as the majority of charge carriers are electrons. In an electric field of 100 $V{\cdot}\mu m^{-1}$, an electric current of μA levels was achieved via field emission [71]. $PdSe_2$ has been demonstrated to be a novel material for application in condensed-matter physics, including spintronics [72] and straintronics [73].

Recently, Lewis acid treatment [74], the adsorption of organic benzyl viologen [57], and elemental substitution [75] via metal–organic chemical vapor deposition have been demonstrated to be effective strategies for manipulating the band structure of 2D materials, based on preliminary studies. The Lewis acid treatment strategy for doping is described as follows. According to the Lewis acid–base theory, substances are categorized into acids and bases based on their ability to accept or donate electron pairs. Bases provide electron pairs, whereas acids accept them. The commonly used Lewis acids are BF_3, $FeCl_3$ [76], $SnCl_4$, $SbCl_5$ [77], and WCl_6 [78]. The widely employed Lewis bases include H_2O, –OH, NH_3 $–NH_2$, and I_2, which possess lone pairs of electrons. The Lewis adduct formation reaction occurs between Lewis acids and Lewis bases (with N in an NH_3 radical), which leads to a charge-transfer complex [76]. Lewis acids, such as trimethyl borane, possess unoccupied orbitals that accept electron pairs from Lewis bases, including NH_3. Eventually, a Lewis adduct ($NH_3{\cdot}BMe_3$) is formed with a dative covalent bond. Lewis acids often serve as hole-injecting dopants in the hole transport layers of organic devices. Overall, they act as p-type dopants. In contrast, cation-exchange reactions occur when Lewis acids are mixed with inorganic compounds. High-valence Sn cations (+4 valence) replace low-valence cations (+3 valence), such as those in In (In_2O_3), thereby achieving p-type doping [79]. Recently, Sn-substituted Pd was employed for the p-type doping of $PdSe_2$ [74]. However, a quantitative evaluation of the impact of the Lewis acid concentration on the doping level has not been conducted thus far.

In this work, the p-type doping level was correlated to the concentration of $SnCl_4$ to develop a Lewis acid model for doping $PdSe_2$ (by immersive soaking). The shift in the threshold gate voltage was utilized as an indicator of the p-doping level, which depicts the doping of graphene and other 2D materials via water or oxygen chemisorption [80]. The drain current was minimized at the threshold gate voltage in the transfer characteristics of the $PdSe_2$-based FET. To the best of our knowledge, this is the first correlation equation obtained by linearly fitting the threshold gate voltage to the doping concentration. In addition, the structures and electrical performances of pristine and Sn-doped $PdSe_2$ were investigated.

2 Results and discussions

First, the pristine $PdSe_2$ film was prepared via metal selenization. The $PdSe_2$ film was prepared by depositing a palladium metal film onto an Si/SiO_2 substrate (Fig. 1(a)), followed by thermal selenization (Fig. 1(b)). Optical microscopy images of the Pd film before and after selenization are shown in Figs. 1(c) and 1(d), respectively. We achieved the synthesis of large-area noble transition metal dichalcogenides (nTMDCs), i.e., $PdSe_2$ over a 4-inch wafer scale.

After selenization, a distinct color change was observed in the Pd membrane, indicating a transformation to $PdSe_2$. The formation of $PdSe_2$ was further confirmed using Raman spectroscopy. The Raman spectrum (Fig. 1(e)) exhibits four prominent peaks at 142.1, 202.1, 218.4, and 252.7 cm^{-1}, corresponding to vibration modes of A_g^1, A_g^2, B_{1g}^2, and A_g^3 of $PdSe_2$, respectively. This result is in agreement with the findings reported in Refs. [81, 82]. Theoretically, six vibration modes (A_g^1, A_g^2, A_g^3, B_{1g}^1, B_{1g}^2, and B_{1g}^3) exist in the $PdSe_2$ lattice; therefore, the Raman spectrum of $PdSe_2$ should show six significant peaks [83]. However, the peaks of the A_g^1 and B_{1g}^1 modes overlapped to form a single peak at 142.1 cm^{-1}. In addition, A_g^3 and B_{1g}^3 peaks are located close to each other such that only a single peak is observed at 252.7 cm^{-1}. Therefore, the Raman spectrum of $PdSe_2$ shows only four peaks [83]. The atomic force microscopy (AFM) height profile analysis revealed the thicknesses of the Pd and $PdSe_2$ films as 5 and 18 nm, respectively (Fig. S1 in the Electronic Supplementary Material (ESM)). The number of $PdSe_2$ layers obtained in this study was ca. 40, estimated by dividing the total thickness by 0.4 nm for each layer [53, 81, 84].

A puckered pentagonal structure, which corresponds to the atomic structure of $PdSe_2$, is observed in the atomic-resolution

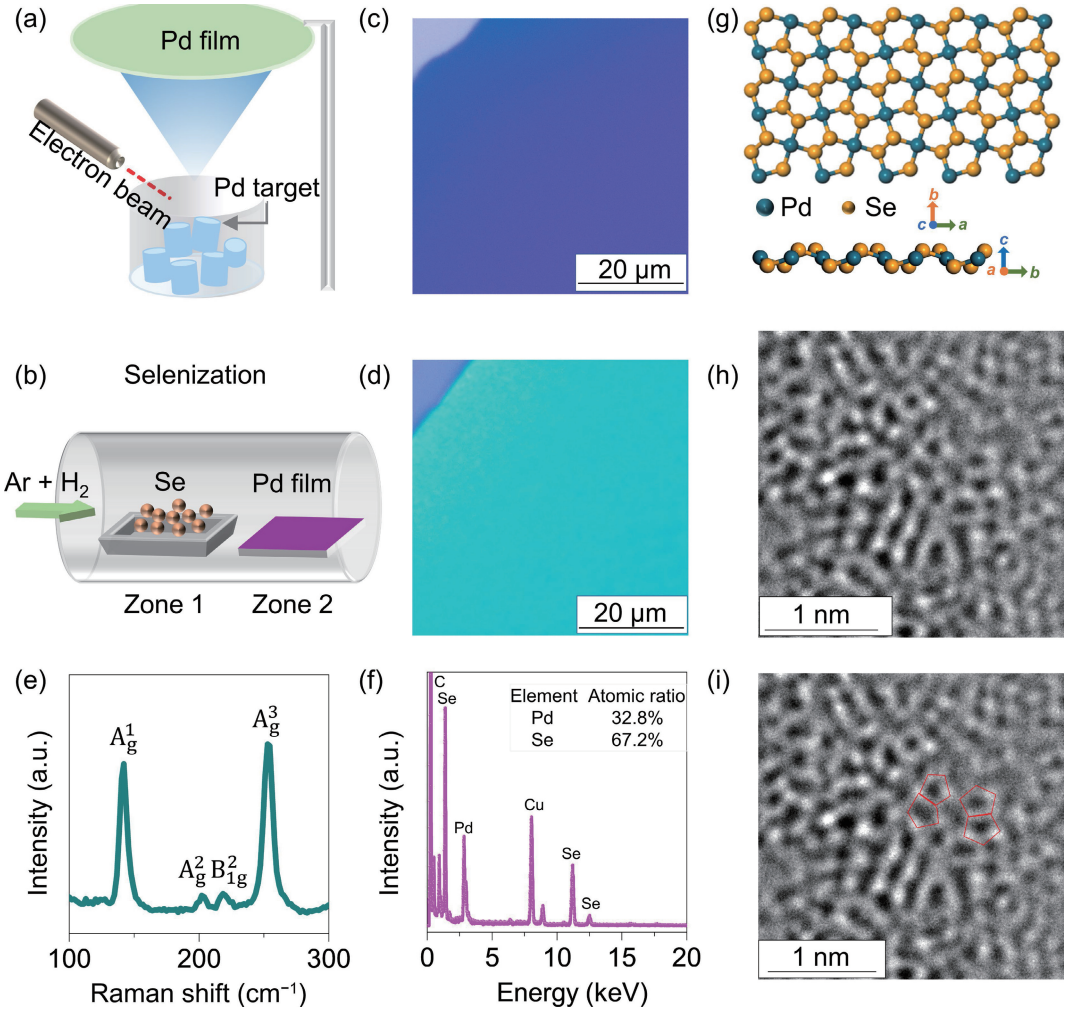

Figure 1 Large-area growth of the $PdSe_2$ full film via selenization. Scheme of synthesis approach: (a) evaporation deposition of the Pd film and (b) selenization. Optical micrographs of (c) Pd and (d) $PdSe_2$ films. (e) Raman spectrum and (f) EDX analysis of the $PdSe_2$ film. (g) Atomic configuration and ((h) and (i)) Cs-corrected atomic-resolution TEM images of $PdSe_2$. Pentagons marked in (i) represent $PdSe_2$ atomic configurations.

transmission electron microscopy (TEM) image [85, 86], confirming the formation of $PdSe_2$. The $PdSe_2$ film was then transferred onto the TEM grid for low-magnification imaging (Fig. S2(a) in the ESM). In addition, the formation of $PdSe_2$ was characterized via an energy-dispersive X-ray (EDX) spectroscopy system, integrated into the TEM chamber (Fig. S2(c) in the ESM). The atomic ratio of Pd to Se (1:2, Fig. 1(f)) in the sample was consistent with the stoichiometric ratio of $PdSe_2$ [67, 74, 87]. High-resolution TEM analysis revealed the lattice structure of $PdSe_2$ with a (211) orientation and a *d* spacing of 0.244 nm (Fig. S2(b) in the ESM). Figure 1(g) shows the atomic configuration of $PdSe_2$. Figures 1(h) and 1(i) show Cs-corrected atomic-resolution TEM images of $PdSe_2$, which are analogous to previous reports. In Fig. 1(i), the $PdSe_2$ atomic configuration is marked using pentagons.

The doped $PdSe_2$ film was analyzed after the initial $SnCl_4$ soaking treatment. By mixing $SnCl_4$ with ethanol to a concentration of 60 μL·mL^{-1}, the obtained $SnCl_4$ solution was dropped onto the $PdSe_2$ film (Fig. 2(a)). Compared to pristine $PdSe_2$ (Fig. 2(b)), Sn-doped $PdSe_2$ (Fig. 2(c)) turned to a light-yellow color from cyan, as observed via optical microscopy. Therefore, the doping mechanism should be evaluated. $SnCl_4$ can interact with $PdSe_2$ in two ways: via molecular doping with $SnCl_4$ (physisorption and chemisorption) or ionic exchange reactions (Sn^{4+} substituting Pd^{2+}). AFM and Raman analyses were employed to determine the doping type, that is, to explore whether molecular doping occurred via adsorption [88, 89] or ion-exchange reactions.

The electron energy loss spectroscopy (EELS), which is often equipped inside a scanning TEM (STEM) equipment, provides chemical environmental information analogous to X-ray spectroscopy (XPS) data. By the electron energy loss spectrum, the emergence of Sn M edge (500–530 eV) at Fig. 2(f) confirms the successful doping of Sn, while Pd M edge (ca. 300 eV) and Se M edge (with an $M_{4,5}$ peak at ca. 57 eV) emerge for both samples, which match the EELS Atlas database (powered by top EELS spectroscopy provider GATAN ametek: https://eels.info/atlas) well.

The Raman peak positions and full-width at half maximum (FWHM) values of the peaks related to the vibration mode were sensitive to doping. Hence, Raman spectral measurements were conducted to characterize the pristine and doped $PdSe_2$ samples.

First, the effect of $SnCl_4$ molecular doping on the treated $PdSe_2$ sample was investigated. The presence of $SnCl_4$ residues on the sample surface after rinsing in organic solvents (noted in the experimental details of the $SnCl_4$ treatment) was evaluated, which is an important aspect of this study. The Raman measurements of these samples were within the wavenumber range covering the vibrational modes of the Sn–Cl bond. Based on literature reports, three peaks emerge at 311, 229, and 158 cm^{-1}, corresponding to the three vibration modes of the Sn–Cl bonds, A_g^1, E_g, and F_g^2 [90], respectively. However, no significant peaks were observed for these bands (Fig. S4 in the ESM).

To determine whether a thickness change occurred upon Lewis acid treatment, AFM measurements of the $PdSe_2$ films were

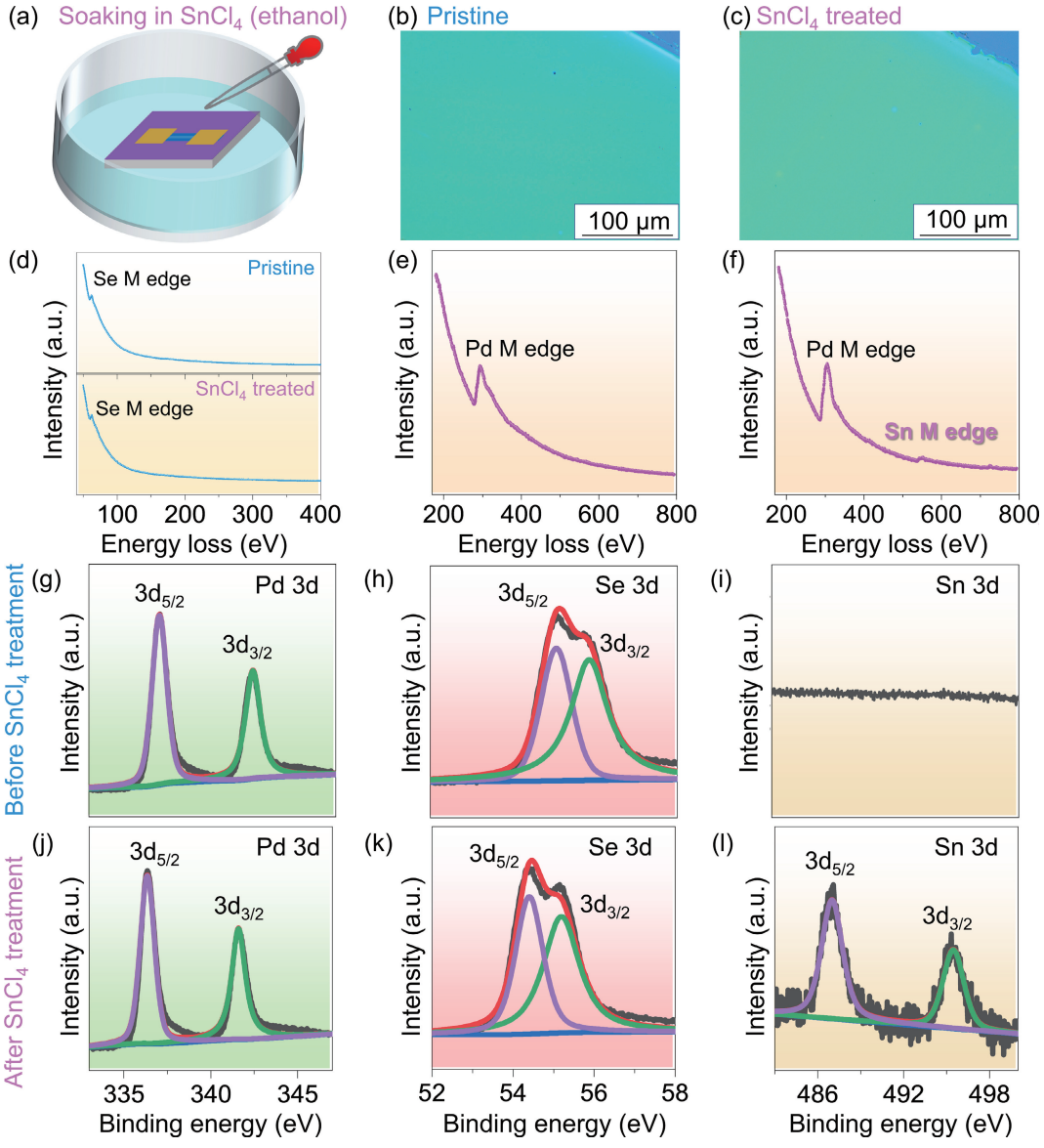

Figure 2 Lewis acid treatment of $PdSe_2$ by $SnCl_4$ soaking. (a) Scheme for the soaking of the $PdSe_2$-channeled transistor in diluted $SnCl_4$ (with ethanol). Optical micrographs of $PdSe_2$ (b) before and (c) after $SnCl_4$ soaking for 30 min. Electron energy loss spectroscopy data for (d) Se, Pd, and Sn in (e) pristine and (f) treated $PdSe_2$ samples. XPS results: (g) Pd 3d, (h) Se 3d, and (i) Sn 3d spectra of the pristine $PdSe_2$ sample. (j) Pd 3d, (k) Se 3d, and (l) Sn 3d peaks of $SnCl_4$-treated specimen.

conducted before and after $SnCl_4$ treatment. The thicknesses of pristine and Sn-doped $PdSe_2$ films did not show any difference (Fig. S5 in the ESM). Both Raman and AFM data confirmed that the doping in this study was not $SnCl_4$ molecular doping. Therefore, rinsing with organic solvents does not recover the p-doping level of the samples to that of pristine $PdSe_2$.

Next, the accuracy of the hypothesis that Sn replaced Pd in an ionic exchange reaction was investigated. The vibration peaks of the Sn–Se bond were detected at 180 cm^{-1} (Fig. S6 in the ESM), which corresponds to the A_g^1 mode of $SnSe_2$ [91]. The FWHM of the A_g^3 mode peak of Sn-doped $PdSe_2$ is relatively less than that of pristine $PdSe_2$ (Table S1 in the ESM). Additionally, a red Raman shift is observed (i.e., the peak position shifted to low-wavenumber regions) in the A_g^3 mode. Furthermore, EDX analysis was conducted for evaluating the elemental composition of the pristine and doped samples. For pristine $PdSe_2$, Pd and Se peaks were observed, whereas Sn and Cl peaks were not detected (Fig. S7(a) in the ESM). For Sn-doped $PdSe_2$, an additional peak (3.44 keV) emerged, which was assigned to Sn (Fig. S7(b) in the ESM), whereas no Cl peak appeared (2.62 keV). Therefore, EDX confirmed that the ion-exchange reaction by the Sn-substitution of Pd dominated the underlying chemistry of the treatment.

The samples were further characterized using XPS to verify the changes in surface chemical compositions and electronic structures after $SnCl_4$ doping. Before Sn doping, the spectra of the original $PdSe_2$ sample shows Pd $3d_{5/2}$ (337 eV) and Pd $3d_{3/2}$ (342.3 eV) peaks (Fig. 2(g)), as well as Se $3d_{5/2}$ (55 eV) and Se $3d_{3/2}$ (55.8 eV) peaks (Fig. 2(h)), which are consistent with the characteristic peaks of $PdSe_2$ [47, 54]. Besides, no peak of Sn is observed (Fig. 2(i)). After Sn doping, the spectra of $SnCl_4$-doped samples exhibit Pd $3d_{5/2}$ (336.3 eV) and Pd $3d_{3/2}$ (341.6 eV) peaks (Fig. 2(j)), in addition to Se $3d_{5/2}$ (54.4 eV) and Se $3d_{3/2}$ (55.2 eV) peaks (Fig. 2(k)). Moreover, the peaks of Sn $3d_{5/2}$ and Sn $3d_{3/2}$ emerge at 486.9 and 495.5 eV (Fig. 2(l)). These results confirm that Sn is doped into $PdSe_2$ (Table S2 in the ESM). In addition, the Pd 3d and Se 3d peaks shifted to low binding energies by 0.7 and 0.6 eV, which is consistent with previous reports on p-type doping [75, 92]. The binding energy shift provides the basis for understanding the pathway of charge transfer between $SnCl_4$ and $PdSe_2$, which leads to an increase in the number of $PdSe_2$ valence band hole carriers as observed in the electrical characterization.

Next, the impact of $SnCl_4$ soaking treatment of $PdSe_2$ on the transistor performance was examined. An FET was fabricated (Fig. 3(a)) by placing a $PdSe_2$ film on an SiO_2/Si substrate, and

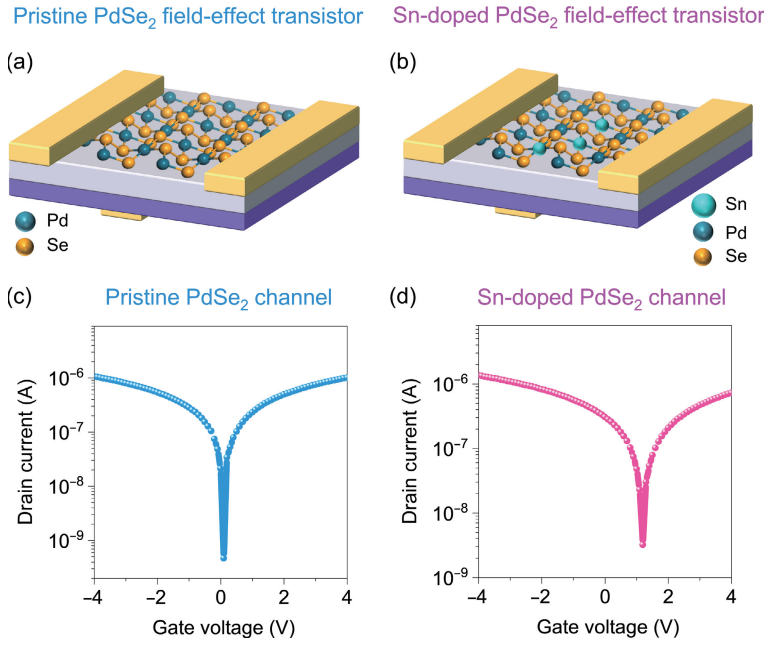

Figure 3 Demonstration of p-type doping of $PdSe_2$ via Lewis acid treatment. Scheme of FETs based on the channel of (a) pristine $PdSe_2$ and (b) treated $PdSe_2$ with Sn substitution. Transfer characteristics of FETs based on (c) pristine $PdSe_2$ and (d) Sn-doped $PdSe_2$. Threshold voltage increases after Lewis acid treatment, indicating p-type doping.

Ti/Au electrodes (5/50 nm) were plated on both ends of the film with a mask plate, which were used as the source and drain electrodes, respectively (Fig. S8 in the ESM). *I*–*V* tests were conducted at different gate voltages (Fig. S9 in the ESM). The typical output current exhibited a linear relationship with the drain voltage. The sweeping of the gate voltage from −8 to +8 V shows a continuous regulation of the channel conductance.

Transfer characteristics were analyzed for the original $PdSe_2$ FET device. The transfer characteristic curve of $PdSe_2$ was obtained at drain-source voltage (V_{DS}) = 0.1 V (Fig. 3(c)). The parabolic transfer curve satisfies quadratic fitting ($y = Ax^2$), indicating that the $PdSe_2$ FET device exhibits bipolar transfer characteristics. Considering the linear range of the transfer curve, the hole and electron mobility values of the pristine $PdSe_2$ transistor are estimated as 359 and 337 $cm^2 \cdot V^{-1} \cdot s^{-1}$, respectively (transistor mobility extraction is detailed in the ESM).

The prepared $PdSe_2$ FET was immersed in 60 $\mu L \cdot mL^{-1}$ of an $SnCl_4$ solution, and thereafter, its performance was measured after drying. The threshold voltage of $PdSe_2$ shifted to a positive gate voltage (Fig. 3(d)), showing typical p-type doping behavior. This p-type doping phenomenon agrees well with doping of other 2D materials such as $PdSe_2$ [81, 93], WSe_2 [94], and PtSSe [95].

The Lewis acid treatment of $PdSe_2$ facilitated the regulation of p-type doping level. Herein, the shifts in the threshold gate voltage are compared for the five $SnCl_4$ concentrations (Fig. 4). The $PdSe_2$ FETs with various levels of doping were considered. $PdSe_2$ FETs doped with 0, 20, 40, 60, and 100 $\mu L \cdot mL^{-1}$ of the $SnCl_4$ solution were analyzed. Similar doping behaviors were observed for all devices. Photographs of the transistor devices are presented in Table S3 in the ESM.

A linear relationship between the threshold voltage shift and the $SnCl_4$ doping concentration was determined. Therefore, linear fitting was conducted, and the relationship between the threshold voltage shift ($\Delta V_{Threshold}$) and doping concentration (c) was obtained as follows

$$\Delta V_{Threshold} = 0.023c - 0.11 \quad (1)$$

where c denotes the doping concentration of $SnCl_4$. The unit for the doping concentration is $\mu L \cdot mL^{-1}$, which represents the amount of $SnCl_4$ in microliters in 1 mL of ethanol. The slope of the curve is 0.023 $V \cdot mL \cdot \mu L^{-1}$, with an intercept of −0.11 V.

The threshold voltages of all the $PdSe_2$ devices doped with $SnCl_4$ are similarly shifted to positive gate voltages, confirming that they are p-doped. In addition, the shift in the threshold voltage has a linear relationship with the doping concentration (Fig. 4(f)). The higher the doping concentration, the larger the shift in the threshold voltage. In the transfer curves (Figs. 4(a)–4(e)), the drain current of the doped $PdSe_2$ slightly decreased compared to that of the original $PdSe_2$ device. The decrease of drain current can be attributed to the scattering of charge carriers caused by the substitutional defect [96]. The field-effect electron and hole mobility values after doping were 351 and 307 $cm^2 \cdot V^{-1} \cdot s^{-1}$, respectively, indicating a high retention ratio of mobility after doping.

The highlights of this work have stemmed from the finding of the linearly dependent doping level versus the doping concentration, which may provide reference for the manipulation of doping of 2D materials. Indeed, the quantitative evaluation of the doping level can be modulated with the concentration of dopants. We provide an equation (Eq. (1)) to follow for the design of doping level.

A possible mechanism of band structure regulation at the doping level was then investigated. To explain the p-type doping mechanism of $PdSe_2$, we simplified the atomic structure versus Fermi level shift relationship by the atomic structure and change in the band structure of pristine $PdSe_2$ (Fig. 5(a)) and doped $PdSe_2$ (Figs. 5(b)–5(d)).

When $SnCl_4$ was dissolved in ethanol, Sn^{4+} was released, providing the Sn ions required to replace the Pd ions (Fig. 5(b)). Therefore, the doping mechanism of Sn-substituted Pd should be evaluated before regulating the doping level. Sn substitution of Pd occurs during a cation-exchange reaction. The valences of these two elements must be analyzed to determine the doping type, that is, whether additional electrons or holes are introduced during this reaction.

Sn has a valence of +4 in $SnCl_4$ [97]. However, the assignment of the valence state of Pd is uncommon. The common Pd-based compounds were investigated. Pd shows a typical +2 valence, which is the most stable valence in both simple inorganic salts,

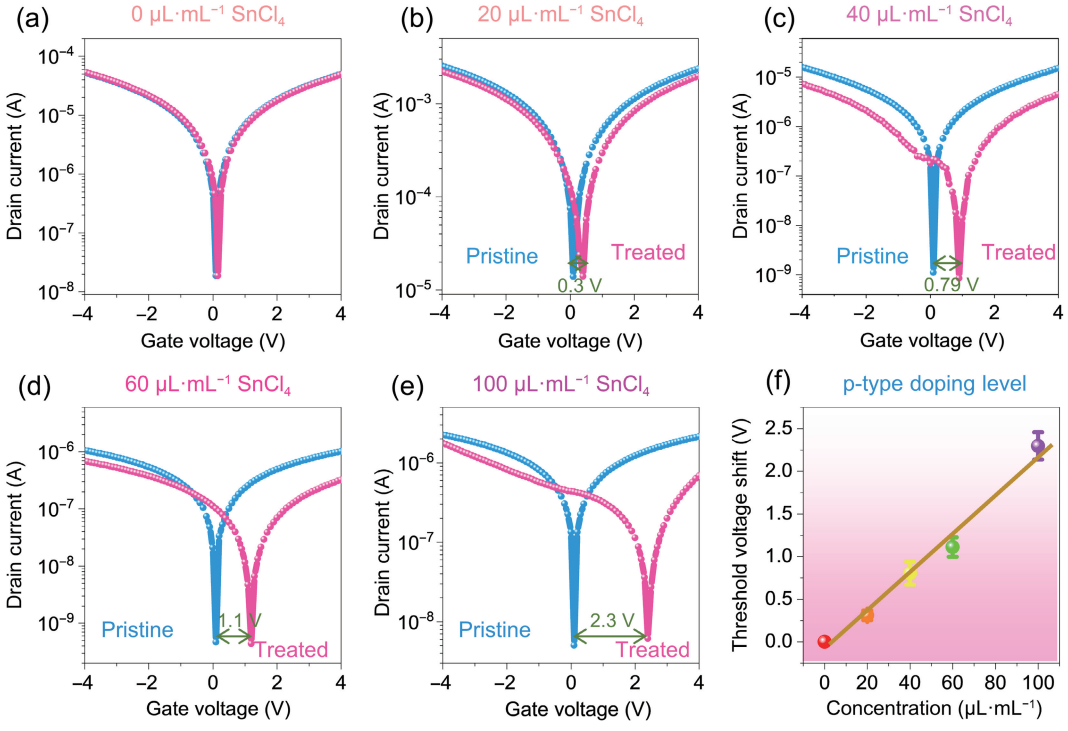

Figure 4 Transfer characteristics of transistors based on different types of $PdSe_2$, and the linear fitting of the threshold voltage shift versus doping concentration of $SnCl_4$ for the $PdSe_2$ treatment. Transfer characteristics of transistors based on pristine $PdSe_2$ and $PdSe_2$ doped (to different levels) with a series of $SnCl_4$ concentrations ranging from ((a)–(e)) 0, 20, 40, 60, and 100 μL·mL^{-1}. (f) Linear fitting of the threshold voltage shift versus the concentration of dopant $SnCl_4$ for $PdSe_2$ treatment. Threshold voltage ($V_{Threshold}$) implies the gate voltage corresponding to the minimum drain current, which is analogous to the Dirac point of graphene-based FETs. $\Delta V_{Threshold}$ represents the shift in the threshold voltage of p-doped $PdSe_2$ with respect to that of pristine $PdSe_2$ owing to Lewis acid treatment.

such as $PdCl_2$, PdS [98], and PdO [99], and coordination complexes, such as $[Pd(CO)_2]^{2+}$ [100] and $Pd(acac)_2$(II) [101].

Recently, Pd was assigned a +2 valence in both PdS_2 and $PdSe_2$ samples [102] via an XPS analysis, where S_2 and Se_2 demonstrated a total charge of −2, i.e., S_2^{2-} and Se_2^{2-}. Therefore, Pd was assigned a +2 valence state in the $PdSe_2$ compound [54]. Pd^{2+}, which may possess an electron configuration of [Kr] $4d^8$ (two electron losses from the 4d orbital $4d^{10}$, data from Encyclopedia of Inorganic Chemistry), was confirmed for $PdSe_2$ by the Berkeley Lab in the Materials Project (a crystal database, No. mp-2418). In addition, Se^- may possess an electron configuration of [Ar] $3d^{10}$ $4s^2$ $4p^5$ (accepting one electron to the 4p orbital, $4p^4$). The lone pair electrons of Se^- occupy the empty orbitals of Pd^{2+}, forming a $PdSe_2$ complex through coordination covalent bonds.

Upon cation exchange [103, 104], Pd^{2+} cations are substituted by Sn^{4+} cations. As a result, additional positive charges are introduced into the lattice system, which shows hole conduction, that is p-type doping. In summary, p-type doping occurs during the Sn substitution of Pd in the $PdSe_2$ lattice.

Besides, selective resonant doping concept was applied to the emerging metal oxyselenide [105]. The proton irradiation provides n doping of 2D materials by incorporation of hydrogen [106] while surface charge transfer also applies [107]. The stacking of 2D materials at different doping levels has led to the proof of the concept photodetector [108] and related photonic circuits [109]. Moreover, the effective doping could break the limit of electronic transport performances of pristine 2D materials [110], which promotes the complementary metal–oxide–semiconductor based integrated circuits [111].

The $PdSe_2$ FET was immersed in $SnCl_4$ solutions of different concentrations (see Experimental section for details). With an increase in the concentration of the $SnCl_4$ solution, the Sn^{4+} concentration increased, along with increasing probability of Sn ion exchange with Pd ions with increasing dopant concentration, which may lead to different levels of doping. Figures 5(a)–5(d) show the atomic structures of pristine $PdSe_2$, along with the atomic structures of $PdSe_2$ treated with increasing concentration of $SnCl_4$. The band structure changes in $PdSe_2$ treated with different concentrations of $SnCl_4$ are shown in Figs. 5(f)–5(h). The Fermi level gradually shifts closer to the valence band maximum (VBM), and the number of hole carriers in the valence band increases, which explains the p-type doping behavior.

The band structure as well as density of states (DOS) of $PdSe_2$ and Sn-doped $PdSe_2$ were calculated, as shown in Fig. 6. The orbital of Sn is strongly hybridized with Pd and Se atoms at the Fermi level, revealing that Sn doping increases the p-type charge carrier concentration.

Device stability is a key parameter for evaluating the long-term applications of a device. The stability of the Sn-doped $PdSe_2$-based FETs using electrical measurements was evaluated, and the as-prepared freshly doped sample was compared with the sample stored for 60 days. The device exhibited a good retention of the transfer curves for p-type doping after 60 days (Fig. S10 in the ESM). In this work, Sn element substitutes Pd in the pristine $PdSe_2$ in a small portion. The doping does not change the crystal structure of $PdSe_2$, which retains the air stability of $PdSe_2$ [54, 68, 112].

During the course of this study, large amount of doping experiments have emerged for catalysis, sensing, and transconductance, including the element N [113], O [114], Br [115], Al [116], Ce [117], Co [118, 119], and V [120]. The transition metals such as V and Nb could be incorporated into 2D materials during [75] or after the chemical vapor deposition process [121, 122]. The doping elements may determine the functional performances of the doped 2D materials such as nanomagnet [123] by Fe doping, catalysis [124] by Pt doping, and superconductivity [125] by Nb doping. More exciting effects of doping of low-dimensional semiconducting materials await further explorations.

The recent advances of $PdSe_2$ come to the defect engineering

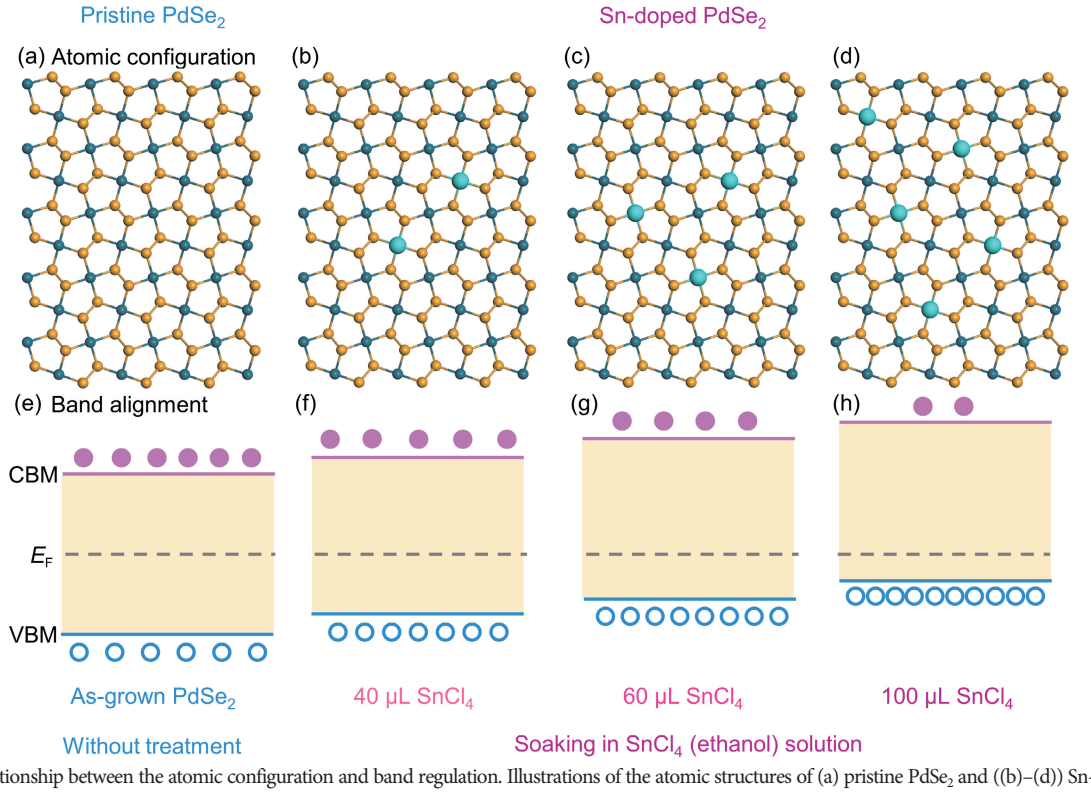

Figure 5 Relationship between the atomic configuration and band regulation. Illustrations of the atomic structures of (a) pristine $PdSe_2$ and ((b)–(d)) Sn-doped $PdSe_2$ with different Sn doping concentrations. Schemes of the band structures of (e) pristine $PdSe_2$ and ((f)–(h)) p-doped $PdSe_2$ with different Sn dopant concentrations. Fermi level of pristine $PdSe_2$ is set as zero. With the Sn substitution of Pd in the $PdSe_2$ lattice, p-type doping occurs, which leads to an increase in the concentration of holes, elevating the valence band maximum. CBM denotes the conductance band minimum.

[126, 127], catalytic sites [128] for electrosynthesis, contact engineering (semiconductor devices) [129–131], nonvolatile memory [132], self-powered photodetectors [133], light-matter interaction [134–136], quantum dots for photovoltaics [137], thermoelectric heat transfer, twistronics [138], and mechanical compressibility [139].

3 Conclusions

In this work, a quantitative approach for the p-type doping of $PdSe_2$ by regulating the concentration of the Lewis acid is reported. Prior to doping, pristine $PdSe_2$ was grown on an Si/SiO_2 substrate via the thermal selenization of a Pd film. The synthesis of $PdSe_2$ was confirmed using optical microscopy, Raman spectroscopy, TEM, and EDX. After Lewis acid treatment, the lattice structure remained unchanged. However, XPS showed emerging peaks of Sn 3d as well as the shift of Pd 3d and Se 3d peaks to low-binding energy regions, confirming the incorporation of Sn as a p-type dopant by substituting Pd. Five concentrations of the $SnCl_4$ solution in ethanol (0, 20, 40, 60, and 100 $\mu L \cdot mL^{-1}$) were employed for doping $PdSe_2$. The results indicate a shift in the threshold voltage (the gate voltage corresponding to the minimum drain current), i.e., an offset voltage of 0.3, 0.8, 1.1, and 2.3 V, for the transistors after doping. Linear fitting of these data leads to the correlation equation $\Delta V_{Threshold} = 0.023c - 0.11$, where c denotes the Lewis acid concentration. The findings of the quantitative evaluation presented herein provide general guidelines for the controllable doping of other 2D materials by regulating the concentration of Lewis acids. This strategy may broaden the choice of p-type 2D materials for assembling van der Waals heterostructures for atomically thin optoelectronic devices.

Two major strategies dominate the doping of low-dimensional semiconductors [140]; viz., one is induced by the environments such as the surface etching [141] and soaking [142], substrate (contact) [143], and physical electrostatic field [144]; and another is composition and structure regulation [145, 146], including superlattice, twisted stacking, later and vertical heterostructures [147], Janus structures, and local intercalations.

Indeed, electrostatic doping [148] remains most frequently employed, which shows chirality tuning [149]. In addition, p-type doping can be achieved by compensating layer for hole injection and Fermi level alignment between metal and semiconductor [150]. Emerging trend relies on the remote charge transfer with an intermediate layer of hexagonal boron nitride (h-BN) to avoid the Coulomb scattering from dopants [151].

To this end, the controlled doping of low-dimensional semiconductors is still at its infant stage. More efforts should be put into this field for reporting more clues to obtain a big picture of controlled doping for wafer-scale homogeneity.

Several p–n junctions have been reported based on $PdSe_2$ and its counterparts, such as MoS_2 [152], $MoSe_2$ [14], $MoTe_2$ [59], WS_2 [153], black phosphorus [154, 155], and other 2D materials [156–158]. Future opportunities could be mined out by revisiting the textbook of the physics of semiconductor devices [159]. Indeed, one can design devices such as current rectifiers [160], photodetectors, solar cells, light-emitting diodes, and lasers, based on the p–n junctions. With the p- and n-type modulation of $PdSe_2$, the possibility of innovation on materials pairing become broader. We expect more upcoming device structures, which provide references in the semiconductor industry.

4 Experimental section

4.1 Growth of the $PdSe_2$ film via metal selenization

First, a Pd film was deposited on Si/SiO_2 wafers using an electron beam evaporation instrument, and then, the Pd film was post-selenized at 380 °C for $PdSe_2$ formation in a horizontal tube furnace in an Ar (135 sccm)/H_2 (15 sccm) atmosphere. Notably,

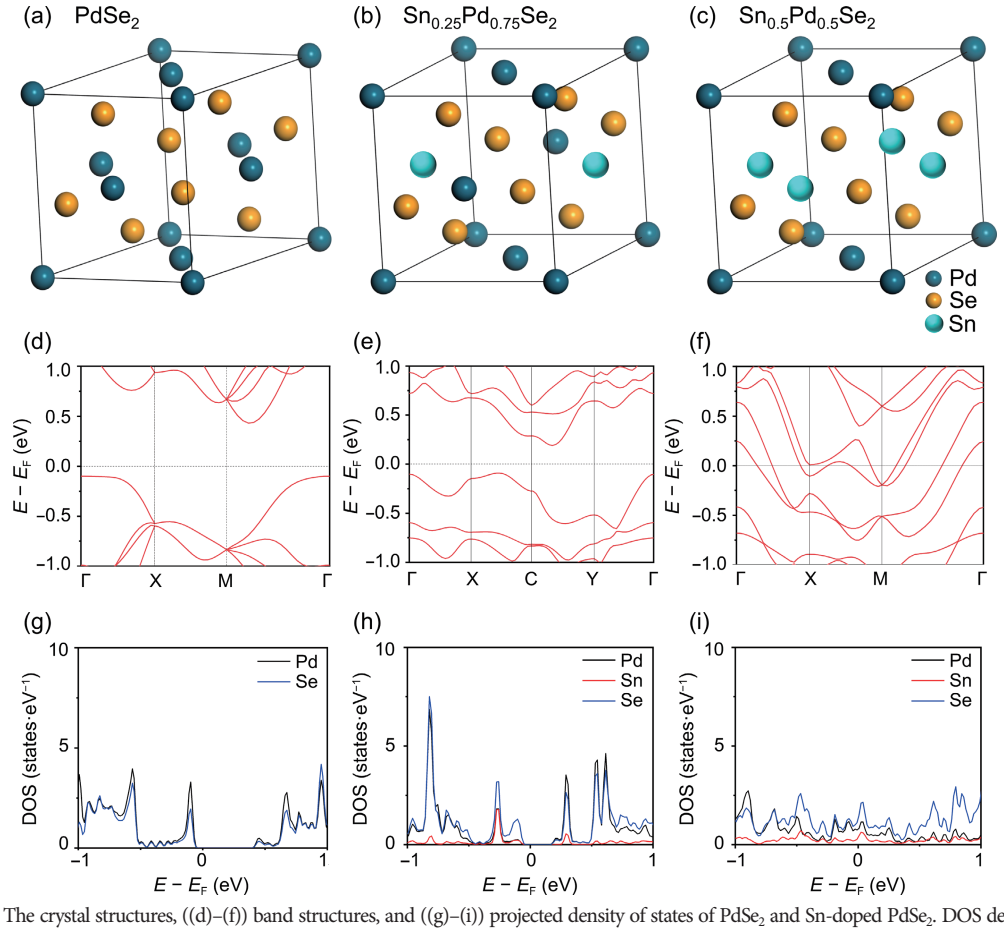

Figure 6 ((a)–(c)) The crystal structures, ((d)–(f)) band structures, and ((g)–(i)) projected density of states of $PdSe_2$ and Sn-doped $PdSe_2$. DOS denotes the density of states.

the thermal deposition approach adopted in this study ensured the homogeneity of large-area 2D materials, and thickness remained constant for all samples. Therefore, simultaneous doping treatments (in the next step) were optimal for investigating the doping strategy of the five types of individual samples considered in this study. In addition, batch experiments with several doping concentrations might avoid operational differences caused by changes in the physical and physiological characteristics of the operators.

4.2 $PdSe_2$ doping by Lewis acid treatment

$SnCl_4$ liquids were dissolved in 10 mL of an ethanol solution at concentrations of 0, 200, 400, 600, and 1000 μL. Thereafter, five types of $SnCl_4$-in-ethanol solutions were prepared with concentrations of 0, 20, 40, 60, and 100 μL·mL^{-1}. Five batches of $PdSe_2$-based transistor devices were immersed in the five $SnCl_4$ solutions for 30 min, respectively. One $PdSe_2$-based device was maintained in an Ar-filled tube (as a reference without any treatment). The devices were then rinsed three times with pure ethanol. Subsequently, the devices were blow-dried using N_2 gas. The devices were stored in Ar-filled tubes for subsequent measurements.

4.3 Materials characterization

Images of the device were obtained using an optical microscope (BX53M; Olympus). Raman spectroscopy was performed using a Raman spectrometer (LabRAM HR Evolution) with a 532 nm laser at room temperature. XPS (Axis Supra) was used to characterize the composition of the samples. A TEM system (FEI Titan Cubed Themis G2 300) with Cs-corrected tools at an acceleration voltage of 80 kV, equipped with a super-X energy-dispersive X-ray spectrometer, was used to analyze the surface morphology, crystal structure, and elemental composition of the samples. In the scanning TEM mode, the electron energy loss spectroscopy was employed for examining the valence states of the elements, with an EELS model, Gatan imaging filter (GIF) quantum detector with electron energy-filtering, and Gatan 894 ultriscan CCD camera.

4.4 Computational section

Crystal structures of heterojunction $PdSe_2$, $Sn_{0.25}Pd_{0.75}Se_2$, and $Sn_{0.5}Pd_{0.5}Se_2$ were constructed by 3 × 3 × 2 supercells with a vacuum spacing of > 15 Å to avoid interaction between adjacent surfaces. All calculations were performed using density functional theory (DFT) in the Perdew–Burke–Ernzerhof (PBE) parameterization of generalized gradient analysis (GGA) and implemented in the Vienna *ab initio* simulation package (VASP) code [161, 162]. The projector augmented wave (PAW) method was used to describe electron–ion interactions. The Brillouin zone (BZ) sampling used a grid spacing of 4 × 4 × 3 and the plane wave basis cutoff was set to 400 eV. Equilibrium geometries were obtained by the minimum energy principle until the energy and force respectively converge to 10^{-4} eV and 0.02 eV·Å^{-1}.

Acknowledgements

J. B. P. thanks the Natural Science Foundation of Shandong Province for Excellent Young Scholars (No. ZR2022YQ41) and the fund (No. SKT2203) from the State Key Laboratories of Transducer Technology, Shanghai Institute of Microsystem and Information Technology, Chinese Academy of Sciences for support. This work was partially supported by the National Key Research and Development Program of China (No. 2022YFE0124200) and the National Natural Science Foundation

of China (No. U2241221). W. J. Z. thanks the Major innovation project of Shandong Province (No. 2021CXGC010603), the National Natural Science Foundation of China (No. 52022037), and the Taishan Scholars Project Special Funds (No. TSQN201812083). The project was supported by the Foundation (No. GZKF202107) of State Key Laboratory of Biobased Material and Green Papermaking, Qilu University of Technology, Shandong Academy of Sciences. M. H. R. thanks the National Natural Science Foundation of China (No. 52071225), the National Science Center and the Czech Republic under the ERDF program "Institute of Environmental Technology—Excellent Research" (No. CZ.02.1.01/0.0/0.0/16_019/0000853), and the Sino-German Research Institute (No. GZ 1400) for support. S. X. H. thanks the National Natural Science Foundation of China (Nos. 21976014 and 22276013) for funding, and thanks the Tianhe2-JK HPC for generous computer time.

Electronic Supplementary Material: Supplementary material (additional information on methods and analysis details) is available in the online version of this article at https://doi.org/10.1007/s12274-023-6196-7.

Funding note: Open Access funding enabled and organized by Projekt DEAL.

References

[1] Jiang, S. W.; Li, L. Z.; Wang, Z. F.; Shan, J.; Mak, K. F. Spin tunnel field-effect transistors based on two-dimensional van der Waals heterostructures. *Nat. Electron.* **2019**, *2*, 159–163.

[2] Zhang, Z.; Lin, P.; Liao, Q. L.; Kang, Z.; Si, H. N.; Zhang, Y. Graphene-based mixed-dimensional van der Waals heterostructures for advanced optoelectronics. *Adv. Mater.* **2019**, *31*, 1806411.

[3] Zhang, S. Y.; Hill, H. M.; Moudgil, K.; Richter, C. A.; Hight Walker, A. R.; Barlow, S.; Marder, S. R.; Hacker, C. A.; Pookpanratana, S. J. Controllable, wide-ranging n-doping and p-doping of monolayer group 6 transition-metal disulfides and diselenides. *Adv. Mater.* **2018**, *30*, 1802991.

[4] Liang, Q. J.; Zhang, Q.; Zhao, X. X.; Liu, M. Z.; Wee, A. T. S. Defect engineering of two-dimensional transition-metal dichalcogenides: Applications, challenges, and opportunities. *ACS Nano* **2021**, *15*, 2165–2181.

[5] Zheng, Y. J.; Chen, Y. F.; Huang, Y. L.; Gogoi, P. K.; Li, M. Y.; Li, L. J.; Trevisanutto, P. E.; Wang, Q. X.; Pennycook, S. J.; Wee, A. T. S. et al. Point defects and localized excitons in 2D WSe_2. *ACS Nano* **2019**, *13*, 6050–6059.

[6] Zheng, Y. J.; Huang, Y. L.; Chen, Y. E.; Zhao, W. J.; Eda, G.; Spataru, C. D.; Zhang, W. J.; Chang, Y. H.; Li, L. J.; Chi, D. Z. et al. Heterointerface screening effects between organic monolayers and monolayer transition metal dichalcogenides. *ACS Nano* **2016**, *10*, 2476–2484.

[7] Yin, X. M.; Wang, Q. X.; Cao, L.; Tang, C. S.; Luo, X.; Zheng, Y. J.; Wong, L. M.; Wang, S. J.; Quek, S. Y.; Zhang, W. J. et al. Tunable inverted gap in monolayer quasi-metallic MoS_2 induced by strong charge-lattice coupling. *Nat. Commun.* **2017**, *8*, 486.

[8] Zhang, W. J.; Wang, Q. X.; Chen, Y.; Wang, Z.; Wee, A. T. S. Van der Waals stacked 2D layered materials for optoelectronics. *2D Mater.* **2016**, *3*, 022001.

[9] Feng, S.; Zou, C. J.; Cong, C. X.; Shang, J. Z.; Zhang, J.; Chen, Y.; Wu, L. S.; Zhang, H. B.; Huang, Z. M.; Gao, W. B. et al. Deterministic and scalable generation of exciton emitters in 2D semiconductor nanodisks. *Adv. Opt. Mater.* **2022**, *10*, 2102702.

[10] Yang, W. H.; Shang, J. Z.; Wang, J. P.; Shen, X. N.; Cao, B. C.; Peimyoo, N.; Zou, C. J.; Chen, Y.; Wang, Y. L.; Cong, C. X. et al. Electrically tunable valley-light emitting diode (vLED) based on CVD-grown monolayer WS_2. *Nano Lett.* **2016**, *16*, 1560–1567.

[11] Pospischil, A.; Furchi, M. M.; Mueller, T. Solar-energy conversion and light emission in an atomic monolayer p–n diode. *Nat. Nanotechnol.* **2014**, *9*, 257–261.

[12] Liu, Y. D.; Cai, Y. Q.; Zhang, G.; Zhang, Y. W.; Ang, K. W. Al-doped black phosphorus p–n homojunction diode for high performance photovoltaic. *Adv. Funct. Mater.* **2017**, *27*, 1604638.

[13] Shang, J. Z.; Cong, C. X.; Wu, L. S.; Huang, W.; Yu, T. Light sources and photodetectors enabled by 2D semiconductors. *Small Methods* **2018**, *2*, 1800019.

[14] Zhong, J. H.; Wu, B.; Madoune, Y.; Wang, Y. P.; Liu, Z. W.; Liu, Y. P. $PdSe_2/MoSe_2$ vertical heterojunction for self-powered photodetector with high performance. *Nano Res.* **2022**, *15*, 2489–2496.

[15] Zhang, Q.; Wang, W. J.; Zhang, J. Q.; Zhu, X. H.; Zhang, Q. Q.; Zhang, Y. J.; Ren, Z. M.; Song, S. S.; Wang, J. M.; Ying, Z. H. et al. Highly efficient photocatalytic hydrogen evolution by ReS_2 via a two-electron catalytic reaction. *Adv. Mater.* **2018**, *30*, 1707123.

[16] Zhang, Q.; Tan, S. J.; Mendes, R. G.; Sun, Z. T.; Chen, Y. T.; Kong, X.; Xue, Y. H.; Rümmeli, M. H.; Wu, X. J.; Chen, S. L. et al. Extremely weak van der Waals coupling in vertical ReS_2 nanowalls for high-current-density lithium-ion batteries. *Adv. Mater.* **2016**, *28*, 2616–2623.

[17] Xue, Y. H.; Zhang, Q.; Wang, W. J.; Cao, H.; Yang, Q. H.; Fu, L. Opening two-dimensional materials for energy conversion and storage: A concept. *Adv. Energy Mater.* **2017**, *7*, 1602684.

[18] Wang, W. J.; Zhang, J. Q.; Zhang, Q.; Wan, S. Y.; Zhu, X. H.; Zhang, Q. Q.; Wang, W. Y.; Zhang, Y. J.; Liu, Y. J.; Fu, L. Self-adapting wettability of ReS_2 under a constant stimulus. *Adv. Mater.* **2018**, *30*, 1804559.

[19] Zhang, Q.; Zhang, J. Q.; Wan, S. Y.; Wang, W. Y.; Fu, L. Stimuli-responsive 2D materials beyond graphene. *Adv. Funct. Mater.* **2018**, *28*, 1802500.

[20] Zhang, Q.; Wang, W. J.; Zhang, J. Q.; Zhu, X. H.; Fu, L. Thermally induced bending of ReS_2 nanowalls. *Adv. Mater.* **2018**, *30*, 1704585.

[21] Zhang, Q.; Wang, W. J.; Kong, X.; Mendes, R. G.; Fang, L. W.; Xue, Y. H.; Xiao, Y.; Rümmeli, M. H.; Chen, S. L.; Fu, L. Edge-to-edge oriented self-assembly of ReS_2 nanoflakes. *J. Am. Chem. Soc.* **2016**, *138*, 11101–11104.

[22] Zhang, Q.; Ren, Z. M.; Wu, N.; Wang, W. J.; Gao, Y. J.; Zhang, Q. Q.; Shi, J.; Zhuang, L.; Sun, X. N.; Fu, L. Nitrogen-doping induces tunable magnetism in ReS_2. *npj 2D Mater. Appl.* **2018**, *2*, 22.

[23] Zhang, Q.; Fu, L. Novel insights and perspectives into weakly coupled ReS_2 toward emerging applications. *Chem* **2019**, *5*, 505–525.

[24] Li, L.; Dong, J. C.; Geng, D. C.; Li, M. H.; Fu, W.; Ding, F.; Hu, W. P.; Yang, H. Y. Multi-stage anisotropic etching of two-dimensional heterostructures. *Nano Res.* **2022**, *15*, 4909–4915.

[25] Zhang, Q.; He, W. Z.; Li, L.; Geng, D. C.; Xu, Z. P.; Chen, H. P.; Chen, W.; Hu, W. P. Oxygen-assisted anisotropic chemical etching of $MoSe_2$ for enhanced phototransistors. *Chem. Mater.* **2022**, *34*, 4212–4223.

[26] Geng, D. C.; Abdelwahab, I.; Xiao, X. F.; Cernescu, A.; Fu, W.; Giannini, V.; Maier, S. A.; Li, L.; Hu, W. P.; Loh, K. P. et al. One-

pot confined epitaxial growth of 2D heterostructure arrays. *ACS Mater. Lett.* **2021**, *3*, 217–223.
[27] Zhang, R. J.; Li, M. H.; Li, L.; Wei, Z. M.; Jiao, F.; Geng, D. C.; Hu, W. P. The more, the better-recent advances in construction of 2D multi-heterostructures. *Adv. Funct. Mater.* **2021**, *31*, 2102049.
[28] Zhang, Q.; Li, E. L.; Wang, Y. S.; Gao, C. S.; Wang, C. Y.; Li, L.; Geng, D. C.; Chen, H. P.; Chen, W.; Hu, W. P. Ultralow-power vertical transistors for multilevel decoding modes. *Adv. Mater.* **2023**, *35*, 2208600.
[29] Zhang, Q.; Geng, D. C.; Hu, W. P. Chemical vapor deposition for few-layer two-dimensional materials. *SmartMat* **2023**, *4*, e1177.
[30] Fan, Y. X.; Li, L.; Zhang, Y.; Zhang, X. T.; Geng, D. C.; Hu, W. P. Recent advances in growth of transition metal carbides and nitrides (MXenes) crystals. *Adv. Funct. Mater.* **2022**, *32*, 2111357.
[31] Fan, Y. X.; Li, L.; Yu, G.; Geng, D. C.; Zhang, X. T.; Hu, W. P. Recent advances in growth of large-sized 2D single crystals on Cu substrates. *Adv. Mater.* **2021**, *33*, 2003956.
[32] Wang, Y. H.; Pang, J. B.; Cheng, Q. L.; Han, L.; Li, Y. F.; Meng, X.; Ibarlucea, B.; Zhao, H. B.; Yang, F.; Liu, H. Y. et al. Applications of 2D-layered palladium diselenide and its van der Waals heterostructures in electronics and optoelectronics. *Nano-Micro Lett.* **2021**, *13*, 143.
[33] Kim, H.; Uddin, S. Z.; Lien, D. H.; Yeh, M.; Azar, N. S.; Balendhran, S.; Kim, T.; Gupta, N.; Rho, Y.; Grigoropoulos, C. P. et al. Actively variable-spectrum optoelectronics with black phosphorus. *Nature* **2021**, *596*, 232–237.
[34] Kim, J.; Baik, S. S.; Ryu, S. H.; Sohn, Y.; Park, S.; Park, B. G.; Denlinger, J.; Yi, Y.; Choi, H. J.; Kim, K. S. Observation of tunable band gap and anisotropic Dirac semimetal state in black phosphorus. *Science* **2015**, *349*, 723–726.
[35] Xie, Z. J.; Hui, L. L.; Wang, J. H.; Zhu, G. A.; Chen, Z. Q.; Li, C. M. Electronic and optical properties of monolayer black phosphorus induced by bi-axial strain. *Comput. Mater. Sci.* **2018**, *144*, 304–314.
[36] Zhang, Y.; Ma, C. Y.; Xie, J. L.; Ågren, H.; Zhang, H. Black phosphorus/polymers: Status and challenges. *Adv. Mater.* **2021**, *33*, 2100113.
[37] He, D. W.; Wang, Y. L.; Huang, Y.; Shi, Y.; Wang, X. R.; Duan, X. F. High-performance black phosphorus field-effect transistors with long-term air stability. *Nano Lett.* **2019**, *19*, 331–337.
[38] Liu, Y. J.; Gao, P. F.; Zhang, T. M.; Zhu, X. J.; Zhang, M. M.; Chen, M. Q.; Du, P. W.; Wang, G. W.; Ji, H. X.; Yang, J. L. et al. Azide passivation of black phosphorus nanosheets: Covalent functionalization affords ambient stability enhancement. *Angew. Chem., Int. Ed.* **2019**, *58*, 1479–1483.
[39] Cai, H. T.; Chin, Y. H. C. Catalytic Effects of chemisorbed sulfur on pyridine and cyclohexene hydrogenation on Pd and Pt clusters. *ACS Catal.* **2021**, *11*, 1684–1705.
[40] Liang, Q. J.; Chen, Z. L.; Zhang, Q.; Wee, A. T. S. Pentagonal 2D transition metal dichalcogenides: $PdSe_2$ and beyond. *Adv. Funct. Mater.* **2022**, *32*, 2203555.
[41] Gu, Y. Y.; Cai, H.; Dong, J. C.; Yu, Y. L.; Hoffman, A. N.; Liu, C. Z.; Oyedele, A. D.; Lin, Y. C.; Ge, Z. Z.; Puretzky, A. A. et al. Two-dimensional palladium diselenide with strong in-plane optical anisotropy and high mobility grown by chemical vapor deposition. *Adv. Mater.* **2020**, *32*, 1906238.
[42] Withanage, S. S.; Khondaker, S. I. Low pressure CVD growth of 2D $PdSe_2$ thin film and its application in $PdSe_2$-$MoSe_2$ vertical heterostructure. *2D Mater.* **2022**, *9*, 025025.
[43] Lu, L. S.; Chen, G. H.; Cheng, H. Y.; Chuu, C. P.; Lu, K. C.; Chen, C. H.; Lu, M. Y.; Chuang, T. H.; Wei, D. H.; Chueh, W. C. et al. Layer-dependent and in-plane anisotropic properties of low-temperature synthesized few-layer $PdSe_2$ single crystals. *ACS Nano* **2020**, *14*, 4963–4972.
[44] Jiang, S. L.; Xie, C. Y.; Gu, Y.; Zhang, Q. H.; Wu, X. X.; Sun, Y. L.; Li, W.; Shi, Y. P.; Zhao, L. Y.; Pan, S. Y. et al. Anisotropic growth and scanning tunneling microscopy identification of ultrathin even-layered $PdSe_2$ ribbons. *Small* **2019**, *15*, 1902789.
[45] Tai, K. L.; Chen, J.; Wen, Y.; Park, H.; Zhang, Q. Y.; Lu, Y.; Chang, R. J.; Tang, P.; Allen, C. S.; Wu, W. W. et al. Phase variations and layer epitaxy of 2D $PdSe_2$ grown on 2D monolayers by direct selenization of molecular Pd precursors. *ACS Nano* **2020**, *14*, 11677–11690.
[46] Nguyen, G. D.; Oyedele, A. D.; Haglund, A.; Ko, W.; Liang, L. B.; Puretzky, A. A.; Mandrus, D.; Xiao, K.; Li, A. P. Atomically precise $PdSe_2$ pentagonal nanoribbons. *ACS Nano* **2020**, *14*, 1951–1957.
[47] Liang, Q. J.; Zhang, Q.; Gou, J.; Song, T. T.; Arramel; Chen, H.; Yang, M.; Lim, S. X.; Wang, Q. X.; Zhu, R. et al. Performance improvement by ozone treatment of 2D $PdSe_2$. *ACS Nano* **2020**, *14*, 5668–5677.
[48] Shautsova, V.; Sinha, S.; Hou, L. L.; Zhang, Q. Y.; Tweedie, M.; Lu, Y.; Sheng, Y. W.; Porter, B. F.; Bhaskaran, H.; Warner, J. H. Direct laser patterning and phase transformation of 2D $PdSe_2$ films for on-demand device fabrication. *ACS Nano* **2019**, *13*, 14162–14171.
[49] Oyedele, A. D.; Yang, S. Z.; Feng, T. L.; Haglund, A. V.; Gu, Y. Y.; Puretzky, A. A.; Briggs, D.; Rouleau, C. M.; Chisholm, M. F.; Unocic, R. R. et al. Defect-mediated phase transformation in anisotropic two-dimensional $PdSe_2$ crystals for seamless electrical contacts. *J. Am. Chem. Soc.* **2019**, *141*, 8928–8936.
[50] Das, T.; Seo, D.; Seo, J. E.; Chang, J. Tunable current transport in $PdSe_2$ via layer-by-layer thickness modulation by mild plasma. *Adv. Electron. Mater.* **2020**, *6*, 2000008.
[51] Hoffman, A. N.; Gu, Y. Y.; Tokash, J.; Woodward, J.; Xiao, K.; Rack, P. D. Layer-by-layer thinning of $PdSe_2$ flakes via plasma induced oxidation and sublimation. *ACS Appl. Mater. Interfaces* **2020**, *12*, 7345–7350.
[52] Xu, W. T.; Jiang, J. Y.; Ma, H. F.; Zhang, Z. W.; Li, J.; Zhao, B.; Wu, R. X.; Yang, X. D.; Zhang, H. M.; Li, B. L. et al. Vapor phase growth of two-dimensional $PdSe_2$ nanosheets for high-photoresponsivity near-infrared photodetectors. *Nano Res.* **2020**, *13*, 2091–2097.
[53] Li, E.; Wang, D. F.; Fan, P.; Zhang, R. Z.; Zhang, Y. Y.; Li, G.; Mao, J. H.; Wang, Y. L.; Lin, X.; Du, S. X. et al. Construction of bilayer $PdSe_2$ on epitaxial graphene. *Nano Res.* **2018**, *11*, 5858–5865.
[54] Hoffman, A. N.; Gu, Y. Y.; Liang, L. B.; Fowlkes, J. D.; Xiao, K.; Rack, P. D. Exploring the air stability of $PdSe_2$ via electrical transport measurements and defect calculations. *npj 2D Mater. Appl.* **2019**, *3*, 50.
[55] Gu, Y. Y.; Zhang, L. Z.; Cai, H.; Liang, L. B.; Liu, C. Z.; Hoffman, A.; Yu, Y. L.; Houston, A.; Puretzky, A. A.; Duscher, G. et al. Stabilized synthesis of 2D verbeekite: Monoclinic $PdSe_2$ crystals with high mobility and in-plane optical and electrical anisotropy. *ACS Nano* **2022**, *16*, 13900–13910.
[56] Lei, W.; Zhang, S. L.; Heymann, G.; Tang, X.; Wen, J. F.; Zheng, X. J.; Hu, G. H.; Ming, X. A new 2D high-pressure phase of $PdSe_2$ with high-mobility transport anisotropy for photovoltaic applications. *J. Mater. Chem. C* **2019**, *7*, 2096–2105.
[57] Withanage, S. S.; Chamlagain, B.; Johnston, A. C.; Khondaker, S. I. Charge transfer doping of 2D $PdSe_2$ thin film and its application in fabrication of heterostructures. *Adv. Electron. Mater.* **2021**, *7*, 2001057.
[58] Wang, H. Y.; Li, Z. X.; Li, D. Y.; Xu, X.; Chen, P.; Pi, L. J.; Zhou, X.; Zhai, T. Y. Junction field-effect transistors based on $PdSe_2$/MoS_2 heterostructures for photodetectors showing high responsivity and detectivity. *Adv. Funct. Mater.* **2021**, *31*, 2106105.
[59] Afzal, A. M.; Iqbal, M. Z.; Dastgeer, G.; Ahmad, A. U.; Park, B. Highly sensitive, ultrafast, and broadband photo-detecting field-effect transistor with transition-metal dichalcogenide van der Waals heterostructures of $MoTe_2$ and $PdSe_2$. *Adv. Sci.* **2021**, *8*, 2003713.
[60] Li, G.; Yin, S. Q.; Tan, C. Y.; Chen, L. J.; Yu, M. X.; Li, L.; Yan, F. Fast photothermoelectric response in CVD-grown $PdSe_2$ photodetectors with in-plane anisotropy. *Adv. Funct. Mater.* **2021**, *31*, 2104787.
[61] Zhang, H. N.; Ma, P. F.; Zhu, M. X.; Zhang, W. F.; Wang, G. M.; Fu, S. G. Palladium selenide as a broadband saturable absorber for ultra-fast photonics. *Nanophotonics* **2020**, *9*, 2557–2567.
[62] Xu, N. N.; Wang, H. F.; Zhang, H. N.; Guo, L. G.; Shang, X. X.; Jiang, S. Z.; Li, D. W. Palladium diselenide as a direct absorption

saturable absorber for ultrafast mode-locked operations: From all anomalous dispersion to all normal dispersion. *Nanophotonics* **2020**, *9*, 4295–4306.

[63] Ye, C. Y.; Yang, Z. Q.; Dong, J. H.; Huang, Y. F.; Song, M. M.; Sa, B.; Zheng, J. Y.; Zhan, H. B. Layer-tunable nonlinear optical characteristics and photocarrier dynamics of 2D $PdSe_2$ in broadband spectra. *Small* **2021**, *17*, 2103938.

[64] Chen, X.; Huang, J. W.; Chen, C. D.; Chen, M. L.; Hu, G. H.; Wang, H. Q.; Dong, N. N.; Wang, J. Broadband nonlinear photoresponse and ultrafast carrier dynamics of 2D $PdSe_2$. *Adv. Opt. Mater.* **2022**, *10*, 2101963.

[65] Wu, J. H.; Ma, H.; Zhong, C. Y.; Wei, M. L.; Sun, C. L.; Ye, Y. T.; Xu, Y.; Tang, B.; Luo, Y.; Sun, B. S. et al. Waveguide-integrated $PdSe_2$ photodetector over a broad infrared wavelength range. *Nano Lett.* **2022**, *22*, 6816–6824.

[66] Wu, D.; Xu, M. M.; Zeng, L. H.; Shi, Z. F.; Tian, Y. Z.; Li, X. J.; Shan, C. X.; Jie, J. S. *In situ* fabrication of $PdSe_2$/GaN schottky junction for polarization-sensitive ultraviolet photodetection with high dichroic ratio. *ACS Nano* **2022**, *16*, 5545–5555

[67] Dong, Z.; Yu, W. Z.; Zhang, L. B.; Mu, H. R.; Xie, L.; Li, J.; Zhang, Y.; Huang, L. Y.; He, X. Y.; Wang, L. et al. Highly efficient, ultrabroad $PdSe_2$ phototransistors from visible to terahertz driven by mutiphysical mechanism. *ACS Nano* **2021**, *15*, 20403–20413.

[68] Liang, Q. J.; Wang, Q. X.; Zhang, Q.; Wei, J. X.; Lim, S. X.; Zhu, R.; Hu, J. X.; Wei, W.; Lee, C.; Sow, C. et al. High-performance, room temperature, ultra-broadband photodetectors based on air-stable $PdSe_2$. *Adv. Mater.* **2019**, *31*, 1807609.

[69] Di Bartolomeo, A.; Pelella, A.; Liu, X. W.; Miao, F.; Passacantando, M.; Giubileo, F.; Grillo, A.; Iemmo, L.; Urban, F.; Liang, S. J. Pressure-tunable ambipolar conduction and hysteresis in thin palladium diselenide field effect transistors. *Adv. Funct. Mater.* **2019**, *29*, 1902483.

[70] Di Bartolomeo, A.; Urban, F.; Pelella, A.; Grillo, A.; Passacantando, M.; Liu, X.; Giubileo, F. Electron irradiation of multilayer $PdSe_2$ field effect transistors. *Nanotechnology* **2020**, *31*, 375204.

[71] Di Bartolomeo, A.; Pelella, A.; Urban, F.; Grillo, A.; Iemmo, L.; Passacantando, M.; Liu, X. W.; Giubileo, F. Field emission in ultrathin $PdSe_2$ back-gated transistors. *Adv. Electron. Mater.* **2020**, *6*, 2000094.

[72] Cheng, P. K.; Tang, C. Y.; Ahmed, S.; Qiao, J. P.; Zeng, L. H.; Tsang, Y. H. Utilization of group 10 2D TMDs-$PdSe_2$ as a nonlinear optical material for obtaining switchable laser pulse generation modes. *Nanotechnology* **2021**, *32*, 055201.

[73] Çakıroğlu, O.; Island, J. O.; Xie, Y.; Frisenda, R.; Castellanos-Gomez, A. An automated system for strain engineering and straintronics of 2D materials. *Adv. Mater. Technol.* **2023**, *8*, 2201091.

[74] Li, Z. X.; Li, D. Y.; Wang, H. Y.; Xu, X.; Pi, L. J.; Chen, P.; Zhai, T. Y.; Zhou, X. Universal p-type doping via lewis acid for 2D transition-metal dichalcogenides. *ACS Nano* **2022**, *16*, 4884–4891.

[75] Kozhakhmetov, A.; Stolz, S.; Tan, A. M. Z.; Pendurthi, R.; Bachu, S.; Turker, F.; Alem, N.; Kachian, J.; Das, S.; Hennig, R. G. et al. Controllable p-type doping of 2D WSe_2 via vanadium substitution. *Adv. Funct. Mater.* **2021**, *31*, 2105252.

[76] Endo, J.; Matsumoto, T.; Kido, J. Organic electroluminescent devices with a vacuum-deposited lewis-acid-doped hole-injecting layer. *Jpn. J. Appl. Phys.* **2002**, *41*, L358–L360.

[77] Ganzorig, C.; Fujihira, M. Improved drive voltages of organic electroluminescent devices with an efficient p-type aromatic diamine hole-injection layer. *Appl. Phys. Lett.* **2000**, *77*, 4211–4213.

[78] Lovchik, M. A.; Pinhas, A. R. The rearrangement of 3-vinylcyclobutene derivatives promoted by metallic Lewis acids. *J. Organomet. Chem.* **2002**, *656*, 299–303.

[79] Morales, E. H.; He, Y. B.; Vinnichenko, M.; Delley, B.; Diebold, U. Surface structure of Sn-doped In_2O_3 (111) thin films by STM. *New J. Phys.* **2008**, *10*, 125030.

[80] Bartolomeo, A. D.; Giubileo, F.; Romeo, F.; Sabatino, P.; Carapella, G.; Iemmo, L.; Schroeder, T.; Lupina, G. Graphene field effect transistors with niobium contacts and asymmetric transfer characteristics. *Nanotechnology* **2015**, *26*, 475202.

[81] Chow, W. L.; Yu, P.; Liu, F. C.; Hong, J. H.; Wang, X. L.; Zeng, Q. S.; Hsu, C. H.; Zhu, C.; Zhou, J. D.; Wang, X. W. et al. High mobility 2D palladium diselenide field-effect transistors with tunable ambipolar characteristics. *Adv. Mater.* **2017**, *29*, 1602969.

[82] Luo, L. B.; Wang, D.; Xie, C.; Hu, J. G.; Zhao, X. Y.; Liang, F. X. $PdSe_2$ multilayer on germanium nanocones array with light trapping effect for sensitive infrared photodetector and image sensing application. *Adv. Funct. Mater.* **2019**, *29*, 1900849.

[83] Oyedele, A. D.; Yang, S. Z.; Liang, L. B.; Puretzky, A. A.; Wang, K.; Zhang, J. J.; Yu, P.; Pudasaini, P. R.; Ghosh, A. W.; Liu, Z. et al. $PdSe_2$: Pentagonal two-dimensional layers with high air stability for electronics. *J. Am. Chem. Soc.* **2017**, *139*, 14090–14097.

[84] Wei, M. Y.; Lian, J.; Zhang, Y.; Wang, C. L.; Wang, Y. M.; Xu, Z. Layer-dependent optical and dielectric properties of centimeter-scale $PdSe_2$ films grown by chemical vapor deposition. *npj 2D Mater. Appl.* **2022**, *6*, 1.

[85] Luo, W. J.; Oyedele, A. D.; Gu, Y. Y.; Li, T. S.; Wang, X. Z.; Haglund, A. V.; Mandrus, D.; Puretzky, A. A.; Xiao, K.; Liang, L. B. et al. Anisotropic phonon response of few-layer $PdSe_2$ under uniaxial strain. *Adv. Funct. Mater.* **2020**, *30*, 2003215.

[86] Wu, Z. H.; Lu, L.; Liang, X. C.; Dun, C.; Yan, S. C.; Mu, E. Z.; Liu, Y.; Hu, Z. Y. Formation of hexagonal $PdSe_2$ for electronics and catalysis. *J. Phys. Chem. C* **2020**, *124*, 10935–10940.

[87] Duan, R. H.; He, Y. C.; Zhu, C.; Wang, X. W.; Zhu, C.; Zhao, X. X.; Zhang, Z. H.; Zeng, Q. S.; Deng, Y.; Xu, M. Z. et al. 2D cairo pentagonal PdPS: Air-stable anisotropic ternary semiconductor with high optoelectronic performance. *Adv. Funct. Mater.* **2022**, *32*, 2113255.

[88] Huang, Y. L.; Zheng, Y. J.; Song, Z. B.; Chi, D. Z.; Wee, A. T. S.; Quek, S. Y. The organic-2D transition metal dichalcogenide heterointerface. *Chem. Soc. Rev.* **2018**, *47*, 3241–3264.

[89] Huang, Y. L.; Wee, A. T. S. The electronic structure at organic-2D material heterointerfaces. *Surf. Rev. Lett.* **2021**, *28*, 2140003.

[90] Hajlaoui, S.; Chaabane, I.; Oueslati, A.; Guidara, K.; Bulou, A. A theoretical study on the molecular structure and vibrational (FT-IR and Raman) spectra of new organic–inorganic compound $[N(C_3H_7)_4]_2SnCl_6$. *Spectrochim. Acta A: Mol. Biomol. Spectrosc.* **2014**, *117*, 225–233.

[91] Du, R. F.; Wang, Y. Z.; Cheng, M.; Wang, P.; Li, H.; Feng, W.; Song, L. Y.; Shi, J. P.; He, J. Two-dimensional multiferroic material of metallic p-doped SnSe. *Nat. Commun.* **2022**, *13*, 6130.

[92] Fan, S. Q.; Tang, X. D.; Zhang, D. H.; Hu, X. D.; Liu, J.; Yang, L. J.; Su, J. Ambipolar and n/p-type conduction enhancement of two-dimensional materials by surface charge transfer doping. *Nanoscale* **2019**, *11*, 15359–15366.

[93] Wu, J.; Zhuge, F. W.; Li, H. Q.; Zhai, T. Y. Recent advances in two-dimensional p-type metal chalcogenides: Synthesis, doping strategies and applications. *J. Phys. D: Appl. Phys.* **2023**, *56*, 023001.

[94] Kim, J. K.; Cho, K.; Jang, J.; Baek, K. Y.; Kim, J.; Seo, J.; Song, M.; Shin, J.; Kim, J.; Parkin, S. S. P. et al. Molecular dopant-dependent charge transport in surface-charge-transfer-doped tungsten diselenide field effect transistors. *Adv. Mater.* **2021**, *33*, 2101598.

[95] Wang, Z.; Xia, H.; Wang, P.; Zhou, X. H.; Liu, C. S.; Zhang, Q. H.; Wang, F.; Huang, M. L.; Chen, S. Y.; Wu, P. S. et al. Controllable doping in 2D layered materials. *Adv. Mater.* **2021**, *33*, 2104942.

[96] Li, M. G.; Wu, X. X.; Guo, W. X.; Liu, Y. L.; Xiao, C.; Ou, T. J.; Zheng, Y.; Wang, Y. W. Controllable p-type doping of monolayer MoS_2 with tantalum by one-step chemical vapor deposition. *J. Mater. Chem. C* **2022**, *10*, 7662–7673.

[97] De Trizio, L.; Li, H. B.; Casu, A.; Genovese, A.; Sathya, A.; Messina, G. C.; Manna, L. Sn cation valency dependence in cation exchange reactions involving $Cu_{2-x}Se$ nanocrystals. *J. Am. Chem. Soc.* **2014**, *136*, 16277–16284.

[98] Gaskell, T. F. The structure of braggite and palladium sulphide. *Z. Kristallogr. Cryst. Mater.* **1937**, *96*, 203–213.

[99] Pace, R. B.; Lardinois, T. M.; Ji, Y. Y.; Gounder, R.; Heintz, O.; Crocker, M. Effects of treatment conditions on Pd speciation in

CHA and beta zeolites for passive NO_x adsorption. *ACS Omega* **2021**, *6*, 29471–29482.

[100] Khivantsev, K.; Jaegers, N. R.; Koleva, I. Z.; Aleksandrov, H. A.; Kovarik, L.; Engelhard, M.; Gao, F.; Wang, Y.; Vayssilov, G. N.; Szanyi, J. Stabilization of super electrophilic Pd^{+2} cations in small-pore SSZ-13 zeolite. *J. Phys. Chem. C* **2020**, *124*, 309–321.

[101] Bondarchuk, I.; Cadete Santos Aires, F. J.; Mamontov, G.; Kurzina, I. Preparation and investigation of Pd and bimetallic Pd-Sn nanocrystals on γ-Al_2O_3. *Crystals* **2021**, *11*, 444.

[102] Selb, E.; Götsch, T.; Janka, O.; Penner, S.; Heymann, G. Crystal structures of the high-pressure palladium dichalcogenides $Pd_{0.94(1)}S_2$ and $Pd_{0.88(1)}Se_2$ comprising exceptional Pd^{IV} oxidation states. *Z. Anorg. Allg. Chem.* **2017**, *643*, 1415–1423.

[103] Santner, S.; Yogendra, S.; Weigand, J. J.; Dehnen, S. Exploring the chemical reaction space at the formation of chalcogenidometalate superspheres in ionic liquids. *Chem.—Eur. J.* **2017**, *23*, 1999–2004.

[104] Yang, X. M.; Wu, L.; Wang, Z.; Bian, J. J.; Lu, T. L.; Zhou, L. P.; Chen, C.; Xu, J. Conversion of dihydroxyacetone to methyl lactate catalyzed by highly active hierarchical Sn-USY at room temperature. *Catal. Sci. Technol.* **2016**, *6*, 1757–1763.

[105] Chen, Y. X.; Qin, W. N.; Mansoor, A.; Abbas, A.; Li, F.; Liang, G. X.; Fan, P.; Muzaffar, M. U.; Jabar, B.; Ge, Z. H.; Zheng, Z. H. Realizing high thermoelectric performance via selective resonant doping in oxyselenide BiCuSeO. *Nano Res.* **2023**, *16*, 1679–1687.

[106] Liang, H. D.; Zheng, Y.; Loh, L.; Hu, Z. H.; Liang, Q. J.; Han, C.; Bosman, M.; Chen, W.; Bettiol, A. A. Robust n-type doping of WSe_2 enabled by controllable proton irradiation. *Nano Res.* **2023**, *16*, 1220–1227.

[107] Zeng, P. Y.; Wang, W. H.; Jiang, J.; Liu, Z.; Han, D. S.; Hu, S. J.; He, J. Y.; Zheng, P.; Zheng, H.; Zheng, L. et al. Thickness-dependent enhanced optoelectronic performance of surface charge transfer-doped ReS_2 photodetectors. *Nano Res.* **2022**, *15*, 3638–3646.

[108] Sun, Y. M.; Xiong, J. X.; Wu, X. M.; Gao, W.; Huo, N. J.; Li, J. B. Highly sensitive infrared polarized photodetector enabled by out-of-plane PSN architecture composing of p-$MoTe_2$, semimetal-$MoTe_2$ and n-$SnSe_2$. *Nano Res.* **2022**, *15*, 5384–5391.

[109] Wang, Y. W.; Zhou, L.; Zhong, M. Z.; Liu, Y. P.; Xiao, S.; He, J. Two-dimensional noble transition-metal dichalcogenides for nanophotonics and optoelectronics: Status and prospects. *Nano Res.* **2022**, *15*, 3675–3694.

[110] Li, H.; Liang, J. K.; Wang, Q. D.; Liu, F. B.; Zhou, G.; Qing, T.; Zhang, S. H.; Lu, J. Device performance limit of monolayer $SnSe_2$ MOSFET. *Nano Res.* **2022**, *15*, 2522–2530.

[111] Li, Z.; Jinkins, K. R.; Cui, D. Z.; Chen, M. R.; Zhao, Z. Y.; Arnold, M. S.; Zhou, C. W. Air-stable n-type transistors based on assembled aligned carbon nanotube arrays and their application in complementary metal-oxide-semiconductor electronics. *Nano Res.* **2022**, *15*, 864–871.

[112] Wu, J.; Zhao, Y. S.; Sun, M. L.; Zheng, M. R.; Zhang, G.; Liu, X. K.; Chi, D. Z. Enhanced photoresponse of highly air-stable palladium diselenide by thickness engineering. *Nanophotonics* **2020**, *9*, 2467–2474.

[113] Qi, S. Y.; Zhang, W. F.; Wang, X. L.; Ding, Y. F.; Zhang, Y.; Qiu, J. K.; Lei, T.; Long, R.; Liu, N. N-doped MoS_2 via assembly transfer on an elastomeric substrate for high-photoresponsivity, air-stable and stretchable photodetector. *Nano Res.* **2022**, *15*, 9866–9874

[114] Liang, Q. J.; Gou, J.; Arramel; Zhang, Q.; Zhang, W. J.; Wee, A. T. S. Oxygen-induced controllable p-type doping in 2D semiconductor transition metal dichalcogenides. *Nano Res.* **2020**, *13*, 3439–3444.

[115] Zhu, Z. Y.; Tiwari, J.; Feng, T. L.; Shi, Z.; Lou, Y.; Xu, B. High thermoelectric properties with low thermal conductivity due to the porous structure induced by the dendritic branching in n-type PbS. *Nano Res.* **2022**, *15*, 4739–4746.

[116] Ullah, S.; Liu, Y.; Hasan, M.; Zeng, W. W.; Shi, Q. T.; Yang, X. Q.; Fu, L.; Ta, H. Q.; Lian, X. Y.; Sun, J. Y. et al. Direct synthesis of large-area Al-doped graphene by chemical vapor deposition: Advancing the substitutionally doped graphene family. *Nano Res.* **2022**, *15*, 1310–1318.

[117] Nan, J. L.; Liu, Y. Q.; Chao, D. Y.; Fang, Y. X.; Dong, S. J. Crystal defect engineering of Bi_2Te_3 nanosheets by Ce doping for efficient electrocatalytic nitrogen reduction. *Nano Res.* **2023**, *16*, 6544–6551.

[118] Zhang, B.; Zhao, Y. G.; Li, L.; Li, Y. K.; Zhang, J.; Shao, G. S.; Zhang, P. Bead-like cobalt-nitrogen co-doped carbon nanocage/carbon nanofiber composite: A high-performance oxygen reduction electrocatalyst for zinc-air batteries. *Nano Res.* **2023**, *16*, 545–554.

[119] Ling, M.; Li, N.; Jiang, B. B.; Tu, R. Y.; Wu, T.; Guan, P. L.; Ye, Y.; Cheong, W. C. M.; Sun, K.; Liu, S. J. et al. Rationally engineered Co and N co-doped WS_2 as bifunctional catalysts for pH-universal hydrogen evolution and oxidative dehydrogenation reactions. *Nano Res.* **2022**, *15*, 1993–2002.

[120] Li, Y. K.; Li, L.; Liu, F. Y.; Wang, B.; Gao, F.; Liu, C.; Fang, J. Y.; Huang, F.; Lin, Z.; Wang, M. Y. Robust route to H_2O_2 and H_2 via intermediate water splitting enabled by capitalizing on minimum vanadium-doped piezocatalysts. *Nano Res.* **2022**, *15*, 7986–7993.

[121] Pam, M. E.; Hu, J. P.; Ang, Y. S.; Huang, S. Z.; Kong, D. Z.; Shi, Y. M.; Zhao, X. X.; Geng, D. C.; Pennycook, S. J.; Ang, L. K. et al. High-concentration niobium-substituted WS_2 basal domains with reconfigured electronic band structure for hydrogen evolution reaction. *ACS Appl. Mater. Interfaces* **2019**, *11*, 34862–34868.

[122] Li, M. G.; Yao, J. D.; Wu, X. X.; Zhang, S. C.; Xing, B. R.; Niu, X. Y.; Yan, X. Y.; Yu, Y.; Liu, Y. L.; Wang, Y. W. p-type doping in large-area monolayer MoS_2 by chemical vapor deposition. *ACS Appl. Mater. Interfaces* **2020**, *12*, 6276–6282.

[123] Li, B.; Xing, T.; Zhong, M. Z.; Huang, L.; Lei, N.; Zhang, J.; Li, J. B.; Wei, Z. M. A two-dimensional Fe-doped SnS_2 magnetic semiconductor. *Nat. Commun.* **2017**, *8*, 1958.

[124] Wang, C.; Furlan de Oliveira, R.; Jiang, K. Y.; Zhao, Y. D.; Turetta, N.; Ma, C.; Han, B.; Zhang, H. M.; Tranca, D.; Zhuang, X. D. et al. Boosting the electronic and catalytic properties of 2D semiconductors with supramolecular 2D hydrogen-bonded superlattices. *Nat. Commun.* **2022**, *13*, 510.

[125] Wan, W.; Harsh, R.; Dreher, P.; de Juan, F.; Ugeda, M. M. Superconducting dome by tuning through a van Hove singularity in a two-dimensional metal. *npj 2D Mater. Appl.* **2023**, *7*, 41.

[126] Jena, T.; Hossain, M. T.; Nath, U.; Sarma, M.; Sugimoto, H.; Fujii, M.; Giri, P. K. Evidence for intrinsic defects and nanopores as hotspots in 2D $PdSe_2$ dendrites for plasmon-free SERS substrate with a high enhancement factor. *npj 2D Mater. Appl.* **2023**, *7*, 8.

[127] Kundu, T.; Pal, B.; Das, B.; Paramanik, R.; Maity, S.; Ghosh, A.; Palit, M.; Kopciuszynski, M.; Barinov, A.; Mahatha, S. K. et al. Tunable electron transport in defect-engineered $PdSe_2$. *Chem. Mater.* **2023**, *35*, 5212–5221.

[128] Yu, Z. Y.; Lv, S. Y.; Yao, Q.; Fang, N.; Xu, Y.; Shao, Q.; Pao, C. W.; Lee, J. F.; Li, G. L.; Yang, L. M. et al. Low-coordinated Pd site within amorphous palladium selenide for active, selective, and stable H_2O_2 electrosynthesis. *Adv. Mater.* **2023**, *35*, 2208101.

[129] Semkin, V. A.; Shabanov, A. V.; Mylnikov, D. A.; Kashchenko, M. A.; Domaratskiy, I. K.; Zhukov, S. S.; Svintsov, D. A. Zero-bias photodetection in 2D materials via geometric design of contacts. *Nano Lett.* **2023**, *23*, 5250–5256.

[130] Wang, Z. P.; Ali, N.; Ngo, T. D.; Shin, H.; Lee, S.; Yoo, W. J. Achieving ultrahigh electron mobility in $PdSe_2$ field-effect transistors via semimetal antimony as contacts. *Adv. Funct. Mater.* **2023**, *33*, 2301651.

[131] Zha, J.; Liu, H. D.; Wang, H. D.; Li, S. Y.; Huang, H. X.; Xia, Y. P.; Ma, C.; Yang, P.; Zhang, Z. M.; Yang, Z. B. et al. Plasma-optimized contact for high-performance $PdSe_2$ nanoflake-based field-effect transistors. *Appl. Phys. Lett.* **2023**, *123*, 042104.

[132] Wang, W. X.; Jin, J. Y.; Wang, Y. R.; Wei, Z.; Xu, Y. S.; Peng, Z. S.; Liu, H.; Wang, Y.; You, J. W.; Impundu, J. et al. High-speed optoelectronic nonvolatile memory based on van der Waals heterostructures. *Small*, in press, https://doi.org/10.1002/smll.202304730.

[133] Zhang, X. R.; Dai, M. J.; Deng, W. J.; Zhang, Y. Z.; Wang, Q. J. A broadband, self-powered, and polarization-sensitive $PdSe_2$ photodetector based on asymmetric van der Waals contacts. *Nanophotonics* **2023**, *12*, 607–618.

[134] Chen, H. L.; Kuklin, A.; Xiao, J.; Al-Hartomy, O. A.; Al-Ghamdi, A.; Wageh, S.; Zhang, Y. L.; Ågren, H.; Gao, L. F.; Zhang, H. Direct observation of photon induced giant band renormalization in 2D $PdSe_2$ dichalcogenide by transient absorption spectroscopy. *Small*, in press, https://doi.org/10.1002/smll.202302760.

[135] Chen, T. H.; Xiao, L.; Liu, Y.; Wang, J. Z.; Wang, X. R.; Wang, X. M.; Yan, S. C.; Shi, Y. Gate-tunable photovoltaic efficiency in graphene-sandwiched $pdse_2$ photodetectors with restrained carrier recombination. *Adv. Opt. Mater.* **2023**, *11*, 2300167.

[136] Zhang, R.; Yang, Z. J.; Liu, L. W.; Lin, J.; Wen, S. F.; Meng, Y.; Yin, Y.; Lan, C. Y.; Li, C.; Liu, Y. et al. Highly sensitive broadband bolometric photodetectors based on 2D $PdSe_2$ thin film. *Adv. Opt. Mater.*, in press, https://doi.org/10.1002/adom.202301055.

[137] Sun, Y. L.; Wei, Z. Q.; Zhao, C. Y.; Zhang, G. P.; Zhang, G. Y.; Zhou, S.; Zhang, Z. Z.; Yu, Y. G.; Zhang, Q.; Li, X. G. et al. $PdSe_2$ quantum dots for improving the photovoltaic performance of nonfullerene organic solar cells. *Sol. RRL* **2023**, *7*, 2200965.

[138] Wang, S. Y.; Li, D. K.; Zha, M. J.; Yan, X. Q.; Liu, Z. B.; Tian, J. G. Tunable optical activity in twisted anisotropic two-dimensional materials. *ACS Nano* **2023**, *17*, 16230–16238.

[139] Jiang, X. X.; Zhang, S. Z.; Jiang, D. Q.; Wang, Y. G.; Molokeev, M. S.; Wang, N. Z.; Liu, Y. Q.; Zhang, X. Y.; Lin, Z. S. Unexpected giant negative area compressibility in palladium diselenide. *Natl. Sci. Rev.* **2023**, *10*, nwad016.

[140] Zhang, S. M.; Deng, X. N.; Wu, Y. F.; Wang, Y. Q.; Ke, S. X.; Zhang, S. S.; Liu, K.; Lv, R. T.; Li, Z. C.; Xiong, Q. H. et al. Lateral layered semiconductor multijunctions for novel electronic devices. *Chem. Soc. Rev.* **2022**, *51*, 4000–4022.

[141] Lee, D.; Choi, Y.; Kim, J.; Kim, J. Recessed-channel WSe_2 field-effect transistor via self-terminated doping and layer-by-layer etching. *ACS Nano* **2022**, *16*, 8484–8492.

[142] Jeong, B. J.; Lee, B.; Choi, K. H.; Sung, D.; Ghods, S.; Lee, J.; Jeon, J.; Cho, S.; Lee, S. H.; Kim, B. J. et al. Controlled bipolar doping of one-dimensional van der Waals $Nb_2Pd_3Se_8$. *Nano Lett.* **2023**, *23*, 6269–6275.

[143] Kwon, G.; Choi, Y. H.; Lee, H.; Kim, H. S.; Jeong, J.; Jeong, K.; Baik, M.; Kwon, H.; Ahn, J.; Lee, E. et al. Interaction- and defect-free van der Waals contacts between metals and two-dimensional semiconductors. *Nat. Electron.* **2022**, *5*, 241–247.

[144] Wang, Y.; Kim, J. C.; Li, Y.; Ma, K. Y.; Hong, S.; Kim, M.; Shin, H. S.; Jeong, H. Y.; Chhowalla, M. p-type electrical contacts for 2D transition-metal dichalcogenides. *Nature* **2022**, *610*, 61–66

[145] Li, M. J.; Liu, H. F.; Zhao, R. Y.; Yang, F. S.; Chen, M. R.; Zhuo, Y.; Zhou, C. W.; Wang, H.; Lin, Y. F.; Yang, J. J. Imperfection-enabled memristive switching in van der Waals materials. *Nat. Electron.* **2023**, *6*, 491–505.

[146] Dong, J. F.; Suwardi, A.; Tan, X. Y.; Jia, N.; Saglik, K.; Ji, R.; Wang, X. Z.; Zhu, Q.; Xu, J. W.; Yan, Q. Y. Challenges and opportunities in low-dimensional thermoelectric nanomaterials. *Mater. Today* **2023**, *66*, 137–157.

[147] Xiong, Y. H.; Xu, D.; Feng, Y. P.; Zhang, G. J.; Lin, P.; Chen, X. p-type 2D semiconductors for future electronics. *Adv. Mater.*, in press, https://doi.org/10.1002/adma.202206939.

[148] Li, Z. Q.; Yan, T. T.; Fang, X. S. Low-dimensional wide-bandgap semiconductors for UV photodetectors. *Nat. Rev. Mater.* **2023**, *8*, 587–603.

[149] Shreiner, R.; Hao, K.; Butcher, A.; High, A. A. Electrically controllable chirality in a nanophotonic interface with a two-dimensional semiconductor. *Nat. Photonics* **2022**, *16*, 330–336.

[150] Cho, Y.; Schleder, G. R.; Larson, D. T.; Brutschea, E.; Byun, K. E.; Park, H.; Kim, P.; Kaxiras, E. Modulation doping of single-layer semiconductors for improved contact at metal interfaces. *Nano Lett.* **2022**, *22*, 9700–9706.

[151] Jang, J.; Kim, J. K.; Shin, J.; Kim, J.; Baek, K. Y.; Park, J.; Park, S.; Kim, Y. D.; Parkin, S. S. P.; Kang, K. et al. Reduced dopant-induced scattering in remote charge-transfer-doped MoS_2 field-effect transistors. *Sci. Adv.* **2022**, *8*, eabn3181.

[152] Mondal, A.; Biswas, C.; Park, S.; Cha, W.; Kang, S. H.; Yoon, M.; Choi, S. H.; Kim, K. K.; Lee, Y. H. Low ohmic contact resistance and high on/off ratio in transition metal dichalcogenides field-effect transistors via residue-free transfer. *Nat. Nanotechnol.*, in press, https://doi.org/10.1038/s41565-023-01497-x.

[153] Kang, X. L.; Lan, C. Y.; Li, F. Z.; Wang, W.; Yip, S.; Meng, Y.; Wang, F.; Lai, Z. X.; Liu, C. Y.; Ho, J. C. van der Waals $PdSe_2/WS_2$ heterostructures for robust high-performance broadband photodetection from visible to infrared optical communication band. *Adv. Opt. Mater.* **2021**, *9*, 2001991.

[154] Dong, Q. S.; Wang, F.; Hu, X.; Lu, Y.; Zhao, D. X.; Zhang, M.; Han, T.; Hou, X. Y.; Wang, S. L.; Long, M. S. et al. High-performance broadband photodetector based on $PdSe_2$/black phosphorus heterodiode. *Appl. Phys. Lett.* **2022**, *120*, 231103.

[155] Afzal, A. M.; Dastgeer, G.; Iqbal, M. Z.; Gautam, P.; Faisal, M. M. High-performance p-BP/n-$PdSe_2$ near-infrared photodiodes with a fast and gate-tunable photoresponse. *ACS Appl. Mater. Interfaces* **2020**, *12*, 19625–19634.

[156] Aftab, S.; Samiya, M.; Liao, W. G.; Iqbal, M. W.; Ishfaq, M.; Ramachandraiah, K.; Ajmal, H. M. S.; Haque, H. M. U.; Yousuf, S.; Ahmed, Z. et al. Switching photodiodes based on (2D/3D) $PdSe_2$/Si heterojunctions with a broadband spectral response. *J. Mater. Chem. C* **2021**, *9*, 3998–4007.

[157] Fu, C.; Xiao, Y. T.; Xing, Y.; Tong, X. W.; Wang, J.; Zhang, Z. X.; Wang, L.; Wu, D.; Luo, L. B. Filterless discrimination of wavelengths in the range from ultraviolet to near-infrared light using two $PdSe_2$/Thin Si/$PdSe_2$ heterojunction photodetectors. *ACS Appl. Mater. Interfaces* **2021**, *13*, 43273–43281.

[158] Zeng, L. H.; Chen, Q. M.; Zhang, Z. X.; Wu, D.; Yuan, H. Y.; Li, Y. Y.; Qarony, W.; Lau, S. P.; Luo, L. B.; Tsang, Y. H. Multilayered $PdSe_2$/perovskite schottky junction for fast, self-powered, polarization-sensitive, broadband photodetectors, and image sensor application. *Adv. Sci.* **2019**, *6*, 1901134.

[159] Sze, S. M.; Li, Y. M.; Ng, K. K. *Physics of Semiconductor Devices*, 4th ed.; John Wiley & Sons: Hoboken, 2021.

[160] Lee, M.; Park, C. Y.; Sim, S.; Lee, K.; Lee, Y. T. Homogeneous palladium diselenide pn-junction diodes for reconfigurable circuit applications. *Adv. Electron. Mater.* **2022**, *8*, 2101282.

[161] Perdew, J. P.; Burke, K.; Ernzerhof, M. Generalized gradient approximation made simple. *Phys. Rev. Lett.* **1996**, *77*, 3865–3868.

[162] Kresse, G.; Furthmüller, J. Efficient iterative schemes for *ab initio* total-energy calculations using a plane-wave basis set. *Phys. Rev. B* **1996**, *54*, 11169–11186.